

A CONNECTION BETWEEN OBSCURATION AND STAR FORMATION IN LUMINOUS QUASARS

CHIEN-TING J. CHEN¹, RYAN C. HICKOX¹, STACEY ALBERTS^{2,3}, CHRIS M. HARRISON⁴, DAVID M. ALEXANDER⁴, ROBERTO ASSEF⁵, MICHAEL J. I. BROWN⁶, AGNESE DEL MORO⁴, WILLIAM R. FORMAN⁷, VAROUJAN GORJIAN⁸, ANDREW D. GOULDING^{7,9}, KEVIN N. HAINLINE¹, CHRISTINE JONES⁷, CHRISTOPHER S. KOCHAN¹⁰, STEPHEN S. MURRAY¹¹, ALEXANDRA POPE², EMMANUEL ROVILOS⁴, AND DANIEL STERN⁸

Accepted for publication in ApJ

ABSTRACT

We present a measurement of the star formation properties of a uniform sample of mid-IR selected, optically unobscured and obscured quasars (QSO1s and QSO2s) in the Boötes survey region. We use a spectral energy distribution (SED) analysis for photometric data spanning optical to far-IR wavelengths to separate the AGN and host galaxy components. We find that when compared to a matched sample of QSO1s, the QSO2s have roughly twice the higher far-IR detection fractions, far-IR fluxes and infrared star formation luminosities ($L_{\text{IR}}^{\text{SF}}$). Correspondingly, we show that the AGN obscured fraction rises from 0.3 to 0.7 between $(4-40) \times 10^{11} L_{\odot}$. We also find evidence associating X-ray absorption with the presence of far-IR emitting dust. Overall, these results are consistent with galaxy evolution models in which quasar obscuration is associated with a dust-enshrouded starburst galaxies.

Subject headings: galaxies: active — quasars:general — galaxies: starburst — infrared: galaxies — X-rays: galaxies

1. INTRODUCTION

Quasars, the most luminous active galactic nuclei (AGNs¹²), have been linked to galaxies with active star formation (SF) ever since the discovery of their observational connection to ultra-luminous infrared galaxies (ULIRGs, galaxies more luminous than $10^{12} L_{\odot}$, e.g. Sanders et al. 1988). One well-studied scenario for massive galaxy evolution posits that gas-rich galaxy major mergers trigger both rapid supermassive black hole (SMBH) accretion and intense SF. This scenario associates the dust-enshrouded starburst with strong nuclear obscuration that is later expelled by the powerful AGN, implying an evolutionary link between unobscured (type 1) and obscured (type 2) quasars (e.g. Di Matteo et al. 2005; Hopkins et al. 2006; Gilli et al. 2007; Somerville et al. 2008; Treister et al. 2009).

On the other hand, the “unification model” of AGN ascribes obscuration of AGNs to different lines of sight through

a dusty “torus” surrounding the SMBH (e.g. Urry & Padovani 1995; Antonucci 1993). This model predicts no difference in host galaxy properties between obscured and unobscured AGNs. To date, it is still a matter of debate whether the obscuration in luminous quasars can be explained solely by the orientation-based unification model or if it is also enhanced due to dust on larger scales throughout the host galaxy. Several studies have shown results supporting a scenario departing from the unification model, such as the enhanced SF activity (e.g. Canalizo & Stockton 2001; Page et al. 2004; Hiner et al. 2009; Brusa et al. 2008; Shan & Chen 2012) and the more disturbed structure (e.g. Lacy et al. 2007b) of the host galaxies of dust-obscured quasars when compared to unobscured quasars. Clustering of different types of AGNs have also shown that obscured AGNs are more strongly clustered than unobscured AGNs (e.g. Hickox et al. 2011; Donoso et al. 2014; DiPompeo et al. 2014). However, other studies have found no significant difference between obscured and unobscured AGN populations in their morphological and SF properties (e.g. Sturm et al. 2006; Zakamska et al. 2006, 2008; Mainieri et al. 2011; Schawinski et al. 2012; Merloni et al. 2014), and the host galaxy star formation rate (SFR) does not distinguish X-ray selected AGNs with different obscuring column densities (e.g. Rovilos et al. 2012; Rosario et al. 2012; Merloni et al. 2014).

Nonetheless, the measurements of SF properties for quasar host galaxies still suffer from selection biases that are often different among various quasar populations. In particular, optical and X-ray selected quasar samples might have different completeness in obscured and unobscured sources due to the attenuation of optical and X-ray radiation by dust and gas. In fact, some studies have suggested that optical surveys might miss $\sim 50\%$ of the AGN population due to both the obscuration and host galaxy contamination in low-luminosity AGNs (e.g. Goulding & Alexander 2009; Goulding et al. 2010). While current X-ray observations probing photons with energy at ~ 10 keV are believed to be less affected by moderate levels of obscuring materials ($N_{\text{H}} < 10^{24} \text{cm}^{-2}$), a significant

¹ Department of Physics and Astronomy, Dartmouth College, 6127 Wilder Laboratory, Hanover, NH 03755, USA; ctchen@dartmouth.edu.

² Department of Astronomy, Amherst, University of Massachusetts, Amherst, MA 01003, USA

³ Steward Observatory, University of Arizona, Tucson, AZ 85721, USA

⁴ Department of Physics, Durham University, South Road, Durham, DH1 3LE, United Kingdom

⁵ Núcleo de Astronomía de la Facultad de Ingeniería, Universidad Diego Portales, Av. Ejército Libertador 441, Santiago, Chile

⁶ School of Physics, Monash University, Clayton 3800, Victoria, Australia.

⁷ Harvard-Smithsonian Center for Astrophysics, 60 Garden Street, Cambridge, MA 02138.

⁸ Jet Propulsion Laboratory, California Institute of Technology, 4800 Oak Grove Dr., Pasadena, CA 91109, USA

⁹ Princeton University, Department of Astrophysical Sciences, Ivy Lane, Princeton, NJ 08544, USA

¹⁰ Department of Astronomy, Ohio State University, 140 West 18th Avenue, Columbus, OH 43210

¹¹ Department of Physics & Astronomy, The Johns Hopkins University, 3400 N. Charles Street, Baltimore, MD 21218.

¹² In this work, we use AGNs as a general nomenclature for all energetically relevant SMBHs. For AGNs with bolometric luminosity larger than $\sim 10^{45} \text{erg s}^{-1}$, we refer to them as quasars (QSOs).

fraction of X-ray AGNs ($\sim 20-50\%$, e.g. Donley et al. 2005; Guainazzi et al. 2005; Park et al. 2010; Alexander et al. 2011; Georgantopoulos et al. 2013; Wilkes et al. 2013) might still be missed due to obscuration that is Compton-thick ($N_H \sim 10^{24} \text{cm}^{-2}$). Although very hard X-ray photons can penetrate Compton-thick obscuration, the previous high energy X-ray surveys are limited to local sources due to the shallow flux limits (e.g. *Swift*/BAT, Burlon et al. 2011 and *INTEGRAL*, Sazonov et al. 2012). While the *NuSTAR* (Harrison et al. 2013) mission opened a new window of high energy X-ray up to 80 keV, the recent studies that used *NuSTAR* to observe heavily obscured AGNs have found that obscuration is still a non-negligible effect even for X-ray photons at such high energy (Stern et al. 2014; Lansbury et al. 2014).

In contrast, mid-IR observations of the reprocessed emission from the obscuring dust can detect heavily obscured AGNs. A number of studies have shown that large populations of AGNs can be selected using the power-law SED shape of AGNs at mid-IR wavelengths (e.g. Lacy et al. 2004; Stern et al. 2005; Hickox et al. 2007; Donley et al. 2012; Assef et al. 2010b). Although these mid-IR color selection criteria cannot avoid some star forming galaxy interlopers and might miss AGNs accreting at lower accretion rates (e.g. Hickox et al. 2009; Donley et al. 2012; Mateos et al. 2013; Hainline et al. 2014; Chung et al. 2014) or AGNs with complicated silicate features in their mid-IR SED (Kirkpatrick et al. 2013), they are effective in selecting both obscured and unobscured AGNs with similar completeness in mid-IR wavelengths. Recent studies have shown that mid-IR selected AGNs can also be separated into obscured and unobscured populations using a simple optical to mid-IR color selection criterion (e.g. Hickox et al. 2007; Donoso et al. 2014; DiPompeo et al. 2014), which can easily be explained by the different level of extinction in the optical emission from the nucleus (e.g. Hickox et al. 2007, H07 hereafter). Therefore, a direct comparison of the host galaxy SF properties of obscured and unobscured sources in a mid-IR selected quasar sample can provide insights to the origin of obscurations in rapidly accreting SMBHs.

In this work, we adopt the mid-IR selected quasar sample from Hickox et al. (2011, H11 hereafter), which is comprised of unobscured and obscured quasars with similar distributions in quasar properties (e.g. redshift and quasar luminosity), thus making it an excellent sample to study the connection between host galaxy properties and quasar obscuration. The quasar sample studied in this work consists of 546 unobscured quasars (QSO1s) and 345 obscured quasars (QSO2s) selected using *Spitzer* mid-IR observations in the Boötes survey region. We utilize the optical spectroscopy from the AGN and Galaxy Evolution Survey (AGES, Kochanek et al. 2012) and the XBoötes *Chandra* X-ray observations (Murray et al. 2005), along with the $250 \mu\text{m}$ data from the Spectral and Photometric Imaging Receiver (SPIRE, Griffin et al. 2010) on board the *Herschel Space Observatory*. With the inclusion of the far-IR photometry in which AGN contributions have been shown to be much smaller than that of the host galaxy (e.g. Netzer et al. 2007; Lacy et al. 2007a; Kirkpatrick et al. 2012; Mullaney et al. 2012; Chen et al. 2013; Del Moro et al. 2013; Drouart et al. 2014), we can use the wealth of multi-wavelength observations in the Boötes field to obtain robust measurements of SFR for luminous quasars and test if they are associated with obscuration.

We also take advantage of this sample to study the cor-

relation between star formation and AGN accretion for the mid-IR QSOs. In galaxy evolution models which suggest that the concurrent growth of AGN and host galaxy occurs during the dust enshrouded galaxy merger phase, different types of quasars represent different stages of galaxy evolution. To date, observational studies on the connection between SFR and AGN accretion rate have not yet shown definitive conclusions. Positive, strong correlations have been found in studies of optically selected type I quasars (e.g. Serjeant & Hatziminaoglou 2009) and type II quasars (e.g. Netzer 2009); while different conclusions have been found in X-ray selected quasars at higher redshift (e.g. Silverman et al. 2009; Mullaney et al. 2012; Rosario et al. 2012). The difference between observed correlations could be driven by various limitations and observational constraints such as sample size (Page et al. 2012; Harrison et al. 2012) or AGN intrinsic variability (e.g. Chen et al. 2013; Hickox et al. 2014). In addition, it is also important to note that AGNs selected with different criteria are hosted by very different host galaxy populations (e.g. Hickox et al. 2009; Griffith & Stern 2010; Goulding et al. 2014) in which the galaxy and SMBH might follow different evolutionary paths. The sample in this work consists of a large number of luminous QSOs including both the unobscured and heavily obscured populations, thus biases due to small number statistics and the exclusion of dust-enshrouded AGNs are small. The bias in the observed SFR-AGN accretion rate relation in AGN host galaxies due to short-term AGN accretion rate stochasticity may also be less significant in luminous quasars (Hickox et al. 2014). Therefore, the SFR-AGN accretion rate correlation for the mid-IR selected quasar populations may shed light on the origin of the concurrent growth of SMBH and galaxy.

This paper is organized as follows: in §2 we describe the multi-wavelength data and the properties of the quasar sample. In §4, we discuss the SED fitting procedures that we used to disentangle the AGN and the host galaxy contributions. In §3, we explore details of the observed far-IR properties of QSO1s and QSO2s. A comparison of the SF luminosity between QSO1s and QSO2s is laid out at §5; The x-ray properties for the QSO2s are discussed in §6 and the AGN obscured fraction as a function of SF luminosity is discussed in §7. A discussion and a summary are given in §8. Throughout the paper, we use the Vega magnitude system and assume a Λ CDM cosmology with $\Omega_m = 0.3$, $\Omega_\Lambda = 0.7$ and $H_0 = 70 \text{ km s}^{-1}$.

2. THE QUASAR SAMPLE

In this section, we discuss the data from the Boötes survey region as well as the quasar selection and classification criteria we adopted.

2.1. Data

The sample studied in this work comes from the 9 deg^2 Boötes survey region covered by the NOAO Deep Wide-Field Survey (NDWFS, Jannuzi & Dey 1999). Boötes is unique among extragalactic surveys because of its large area and the excellent multi-wavelength coverage from space- and ground-based telescopes, which make possible statistical study of the rare luminous AGNs.

In this work, we use the multiwavelength photometry catalog from Brown et al. (private communication), which the same the one used in Chung et al. (2014). This catalog covers the optical to mid-IR bands including the NDWFS optical observations in *B*, *w*, *R*, *I* bands, near-IR photometry from the NOAO NEWFIRM survey (*J*, *H* and *Ks*, Gonzalez et al.

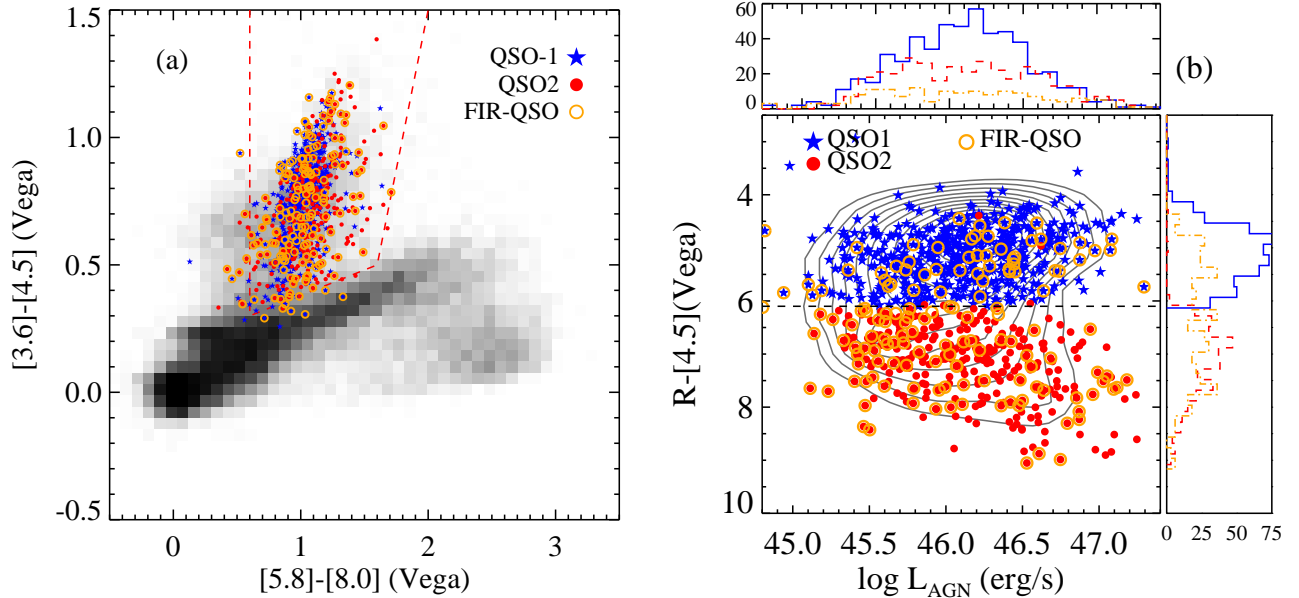


FIG. 1.— (a) IRAC color-color diagram showing the selection of the quasar samples using the criteria of Stern et al. (2005). The gray-scale shows the density of sources detected at $> 5\sigma$ significance in all four bands in SDWFS data. Blue stars and red circles show the QSO1 and QSO2 samples, respectively. The Stern et al. (2005) color-color selection region is shown by the dashed line. In addition, the QSOs with far-IR detections (FIR-QSO) are enclosed with orange circles. Some of the mid-IR QSOs fall out of the selection wedge due to the updated IRAC photometry and aperture corrections (see §2.3). (b) Illustration of the optical-IR color-selection criteria for dividing the IR-selected QSO sample into unobscured (QSO1) and obscured (QSO2) subsamples. Shown is observed $R-[4.5]$ color versus bolometric luminosity, calculated as described in §4. Contours show the distribution for all the Hickox et al. (2007) IR-selected quasars, while blue stars and red circles show the QSO1 and QSO2 subsamples at $0.7 < z < 1.8$ used in H11 and this analysis as described in §2. The distribution in the $R-[4.5]$ color and L_{AGN} are also shown as histograms in the side panels. QSO1s are shown as the blue solid lines, QSO2s are shown as the red dashed lines and the FIR-QSOs are shown as the orange dash-dotted lines. The contours and color histograms show that a simple cut in optical-IR color clearly separates the QSO samples into two populations.

2010) and the *Spitzer* Deep Wide Field Survey (SDWFS, Ashby et al. 2009) of the 4 bands of mid-IR observations from the *Spitzer* Infrared Array Camera (IRAC) at 3.6, 4.5, 5.8 and 8 μm . In addition, the mid-IR photometry from the *Spitzer* Multi-band Imaging Photometer (MIPS) at 24 μm is also included (IRS GTO team, J. Houck (PI), and M. Rieke). In this catalog, the optical to near-IR photometry was extracted from a matched aperture for each band. For B_w , R , I , H and K_s bands, the photometry was measured from images smoothed to a common point spread function (PSF) with a $1''.35$ full width half maximum (FWHM); while for J band, the photometry was measured from images smoothed to a common PSF with a $1''.60$ FWHM. To ensure consistency in the photometry, we use $6''$ aperture photometry from optical bands through the IRAC bands in the mid-IR to account for the large IRAC beam size. For the MIPS data, we use PSF photometry instead of aperture photometry due to the still larger beam size of MIPS. The 5σ flux limits of the optical to near-IR broadband photometry are 25.2, 23.9, 22.9, 21.1, 20.1, 18.9 (Vega magnitudes) for the B_w , R , I , J , H , K_s bands, respectively. For the mid-IR wavelengths, the 5σ flux limits are 6.4, 8.8, 51, 50 and 170 μJy for the 3.6, 4.5, 5.8, 8.0 and 24 μm bands, respectively. A extensive description of the multiband photometry extraction can be found in Brown et al. (2007).

We also make use of the far-IR observations from the publicly available *Herschel* Multi-tiered Extragalactic Survey (HerMES, Oliver et al. 2012). We re-reduced and mosaiced the Boötes SPIRE observations (Alberts et al. 2013), which include a deep $\sim 2 \text{ deg}^2$ inner region near the center of the field and a shallower $\sim 8.5 \text{ deg}^2$ outer region. We specifically focused on removing striping, astrometry offsets, and glitches

missed by the standard pipeline reduction. We also convolved the raw maps with a matched filter (see Chapin et al. 2011), which aided in source extraction by lowering the overall noise and de-blending sources. From this, we generated a matched filter catalog with a 5σ detection threshold. In this catalog, we consider SPIRE sources with fluxes larger than 20 mJy as unambiguously detected. Completeness simulations show that these catalogs are 95% complete in the inner region and 69% complete in the outer regions above a flux of 20 mJy. We also find minimal flux boosting for low SNR sources above this flux cutoff (see S2.2 in Alberts et al. 2013, for the details of the completeness simulation). We match the positions of the SPIRE catalog to the I -band positions with a matching radius of $5''$. We tested the rate of spurious matches by offsetting the SPIRE source positions by $1'$ in a random direction and matching the randomly shifted catalog to the Boötes catalog. We found that with a radius of $5''$, our matching between the SPIRE and Boötes catalog only yielded $< 2\%$ spurious matches.

In addition, we also match the positions of the Brown et al. (2007) catalog to the publicly available *Wide-field Infrared Survey Explorer* (WISE) All-sky catalog (Wright et al. 2010) and obtain the profile-fit photometry magnitudes in the W1, W2, W3 and W4 bands (3.4, 4.6, 12 and 22 μm).

As a complementary measurement of the AGN accretion rate and absorption by gas, we utilize X-ray data from the XBoötes survey, which is a mosaic of 126 short (5 ks) *Chandra* ACIS-I images (Murray et al. 2005; Kenter et al. 2005) covering the entire NDWFS. XBoötes contains 3,293 X-ray point sources with at least four counts in the AGES survey region. The conversion factors from count rates (in counts

s^{-1}) to flux (in erg s^{-1}) for the XBoötes are $6.0 \times 10^{12} \text{ erg s}^{-1} \text{ count}^{-1}$ in the 0.5–2 keV band and $1.9 \times 10^{11} \text{ erg s}^{-1} \text{ count}^{-1}$ in the 2–7 keV band, which are derived for a 5ks on-axis observation and assuming a canonical unabsorbed AGN X-ray spectrum (see §3.3 of Kenter et al. 2005).

For this study, we use spectroscopic redshifts (*spec-zs*) from AGES when possible. For the sources without a *spec-z*, we adopt the photometric redshifts (*photo-zs*) calculated using techniques combining artificial neural network and template fitting algorithms (Brodwin et al. 2006). The uncertainty of this set of *photo-z* is $\sigma = 0.06(1+z)$ for galaxies and $\sigma = 0.12(1+z)$ for AGNs. We note that the uncertainty for AGNs are dominated by the difference between *photo-zs* and *spec-zs* for the type I AGNs. The uncertainties in the *photo-zs* for QSO2s are difficult to estimate accurately as only 9% of the QSO2s have *spec-z* measurements. For these 32 QSO2s, the uncertainty of the *photo-zs* is $\sigma = 0.06(1+z)$, which is consistent with the uncertainty for the galaxy population. Recently spectroscopic follow-up of 35 *WISE*-selected, optically obscured quasars by Hainline et al. (2014) also found that *photo-zs* derived from template-based algorithm (Assef et al. 2010a) have a similar accuracy. This is not surprising since the optical SED for the heavily obscured AGNs is dominated by the host galaxy which has more spectral features and should allow for a more accurate *photo-z* measurement.

An upper limit for the QSO2 *photo-z* uncertainties can be estimated based on different approaches. H07 obtained an uncertainty of $\sigma_z = 0.25(1+z)$ by comparing the Brodwin et al. (2006) *photo-zs* to the *photo-zs* estimated by fitting 3 different galaxy templates to the *B_w*, *R*, *I* photometry. Since the accuracy of the *photo-zs* based on fitting 3 galaxy template to 3 optical photometric observations is limited, the $\sigma_z = 0.25(1+z)$ uncertainty is a very conservative upper limit. For this study, we adopt the *photo-z* uncertainty upper limit of $\sigma_z = 0.25(1+z)$ from H07. However, this is a very conservative estimate since the *photo-z* uncertainties for the QSO2s with host galaxy dominated optical SEDs are likely to be much smaller. A full discussion of the *photo-z* uncertainties is given in §8.

2.2. AGN identification and classification

The AGNs in this work is drawn from the quasar sample of H11, which is a subset of quasars from the H07 mid-IR AGN sample. The H07 AGNs were identified based on the IRAC color-color selection criterion of Stern et al. (2005). For the redshift range of the H07 sample ($0.7 < z \lesssim 3.0$), the IRAC filters probe wavelengths at which the characteristic power-law continuum from the reprocessed AGN radiation starts to dominate. At these wavelengths, the light from old stellar populations is characterized by a Rayleigh-Jeans tail of a blackbody radiation with temperature higher than 2500K, which peaks at wavelengths different than both the AGN accretion disk and the reprocessed AGN emission. In addition, dust emission at near-sublimation temperature heated by the AGN is significantly stronger than that heated by massive stars, thus AGNs can be easily identified with their mid-IR color (e.g. Lacy et al. 2004; Stern et al. 2005; Donley et al. 2012). These reprocessed photons at mid-IR wavelengths are less affected by obscuration than the optical and the X-ray photons due to their much smaller absorption cross section. Therefore, even heavily obscured AGNs can be identified using mid-IR selection criteria.

An important feature of the H07 catalog is that the AGNs were selected from the IRAC Shallow Survey (ISS, Eisenhardt et al. 2004), which has shallower flux limits than

the later SDWFS survey. While the Stern et al. (2005) AGN selection can be contaminated by SF galaxies in deep mid-IR surveys (e.g. Donley et al. 2012), the contamination is negligible at the shallow flux limits of ISS (see Hickox et al. 2007; Assef et al. 2010a, 2011).

H07 also showed that the distribution of the optical (*R*) band to mid-IR (4.5 μm) colors is bimodal for the luminous mid-IR quasars. This bimodality can be easily explained by the difference between the SEDs of unobscured and obscured quasars. For mid-IR selected quasars, the AGN dominates the mid-IR wavelengths, while for obscured quasars, the nuclear emission at optical wavelengths is heavily absorbed. Thus the SED in the *R* band for obscured quasars is similar to those of normal galaxies (e.g. Polletta et al. 2006; Hickox et al. 2007, and Hickox et al. 2014, in preparation). H07 has shown that the mid-IR selected quasars can be separated into two distinct populations of quasars with an empirical color cut at $R - [4.5] = 6.1$. Most ($\sim 80\%$) of the quasars in H07 with $R - [4.5] < 6.1$ are spectroscopically confirmed as type 1 quasars, therefore in this work we refer to these unobscured quasars with $R - [4.5] < 6.1$ as QSO1s. As for quasars with $R - [4.5] > 6.1$, due to the limited depth of AGES, only $\sim 5\%$ have spectroscopic measurements and can be classified as type 2 quasars spectroscopically. However, H07 have extensively studied the quasars with $R - [4.5] > 6.1$ and have shown that these quasars are consistent with bright, obscured X-ray AGNs with $N_{\text{H}} > 10^{22} \text{ cm}^{-2}$ and with AGN bolometric luminosities $L_{\text{AGN}} > 10^{45} \text{ erg s}^{-1}$. Therefore, we refer to the obscured quasars with $R - [4.5] > 6.1$ as QSO2s.

This empirical classification based on the quasar mid-IR to optical color has been shown to be broadly consistent with both the spectroscopically classified sources (Donoso et al. 2014) and X-ray hardness ratio (defined as $HR = (H - S)/(H + S)$ where *H* and *S* are the photon counts in the 2–7 keV band and 0.5–2 keV band, respectively) classification criteria (Hickox et al. 2007; Usman et al. 2014). Since we lack spectroscopic confirmation for the majority of the QSO2s, it is possible that the QSO2s are different than the optical type 2 quasars. Recently, Lacy et al. (2013) have also studied the optical and near-IR spectroscopy of mid-IR AGNs selected using the Donley et al. (2012) IRAC color criteria, and found that a significant fraction ($\sim 33\%$) of the AGNs with evident mid-IR power-law continuum have no significant emission lines consistent with the optical emission line diagnostics (e.g. Baldwin et al. 1981), suggesting that these mid-IR obscured AGNs are more deeply obscured than the optically selected type 2 AGNs. This has also been suggested by the recent study of Hainline et al. (2014).

2.3. The final sample

To minimize the uncertainty in the measurements of quasar and host galaxy properties due to the scattering in the *photo-zs*, we focus on the H11 quasar sample, which is a subsample from H07. The H11 quasar sample focuses on the redshift range $0.7 < z < 1.8$ and limits the QSO1s to those with broad optical emission lines and robust *spec-z* measurements from AGES. For the QSOs in this redshift range, all of the sources have $I < 18$, and the spectroscopic QSO1 sample is highly complete. For the QSO2s in this redshift range, only 32 ($\sim 9\%$) of the QSO2s have *spec-z* measurements. For the rest of QSO2s, we adopt the *photo-zs* from Brodwin et al. (2006). This subset of QSOs have been used in the study of clustering properties of QSO1s and QSO2s in H11, which showed that

in the redshift range $0.7 < z < 1.8$, the sample is highly complete at the shallow flux limits of ISS. The mid-IR selection of this particular sample is shown to suffer less than $< 20\%$ contamination from star-forming galaxies (Hickox et al. 2011). Since the purpose of this work is to compare the star formation properties of QSO1s and QSO2s, it is important to make sure that any difference in SF properties is not driven by the presence of starburst galaxy interlopers. Also, even for bright mid-IR quasars the starburst contribution in the MIR may be non-negligible. Therefore, we rely on SED decompositions to disentangle the AGN and starburst components. The details of the SED decomposition are laid out at §3. Our SED fitting results show that all of the H11 QSOs have a non-negligible ($> 20\%$) AGN component. Based on the SED fitting results, $\sim 3\%$ of the H11 QSOs would have L_{AGN} less than the QSO criterion ($L_{\text{AGN}} > 10^{45} \text{ erg s}^{-1}$). We therefore limit our focus to the sample of 546 QSO1s and 345 QSO2s which satisfies the QSO luminosity criterion and comprise $\sim 97\%$ of the H11 sample.

As a demonstration of the sample used in this work, we show the distribution of the IRAC $[3.6] - [4.5]$ to $[5.8] - [8.0]$ colors and the $R - [4.5]$ to L_{AGN} distributions of the quasar sample in Fig. 1. We note that in Fig. 1a, a small number of the H07 sources have $[3.6] - 4.5$ and $[5.8] - [8.0]$ colors that lie outside the Stern et al. (2005) AGN selection wedge. The Stern et al. (2005) AGN selection wedge and the H07 sample were defined using the original ISS catalog in which the mid-IR photometry was derived using the standard aperture correction, which is different than the PSF profile fitting corrections for individual sources in the Brown et al. (2007) catalog. Moreover, the updated IRAC photometry comes from SDWFS, which is 2 times deeper than the ISS. Thus, it is not surprising that a small fraction ($\sim 4\%$) of the original H07 sample does not meet the original Stern et al. (2005) criterion. However, the QSO sample in Fig. 1a shows a tight $[5.8] - [8.0]$ to $[3.6] - [4.5]$ distribution, which is not seen in the similar Fig. 1a of H11 which use the original ISS photometry. This suggests that the majority of our sample does have power-law like mid-IR SED with the high-precision photometry of SDWFS (e.g. see Fig. 22 in H07). For the purpose of completeness we do not exclude the sources outside of the updated AGN selection wedge, since these sources might still have a non-negligible AGN component which can be identified by the SED fits. However, we note the exclusion of this small fraction of sources has little effect on the average properties of the QSOs. We also show the redshift and flux distributions of the sample in Fig. 2, which shows that the redshift distributions of the QSO1s and QSO2s are similar.

3. SED DECOMPOSITION

Although it is now well-established that far-IR fluxes at wavelengths longer than $60 \mu\text{m}$ in AGN host galaxies are mostly dominated by the emission related to SF (e.g. Netzer et al. 2007; Mullaney et al. 2011; Rosario et al. 2012), caution is still required when estimating the SF properties of powerful quasars. Here we use SED decompositions to ensure that we have reliable estimates of the intrinsic AGN luminosity (L_{AGN}) and star formation luminosity (L_{SF}^{13}).

To properly disentangle the emission from stars and AGN accretion, we fit all of the available broad band photometry in our datasets with SED templates. We combine several empir-

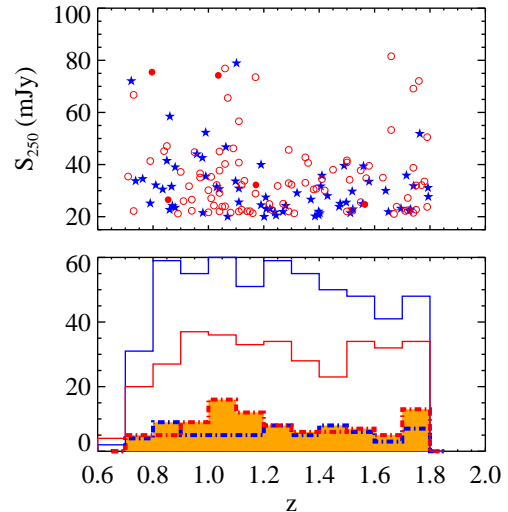


FIG. 2.— *Top*: The $250 \mu\text{m}$ distributions for QSO1s and QSO2s with direct SPIRE detections. QSO1s are shown as the blue stars. The 5 far-IR detected QSO2s with *spec-z* measurements are shown as the filled circles. The rest of the far-IR detected QSO2s with *photo-z*s are shown as open circles. *Bottom*: The redshift distributions of QSO1s and QSO2s are shown in blue and red solid lines. Also shown are the redshift distributions of the QSO1s and QSO2s detected at $250 \mu\text{m}$. The histograms for far-IR detected QSO1s and QSO2s are shown as the blue and red dash-dotted lines and filled in orange. This plot shows that the redshift distributions of QSO1s and QSO2s are similar and QSO2s have more $250 \mu\text{m}$ detections than QSO1s.

ically derived templates to create AGN and host galaxy templates covering the wavelength range from optical to far-IR in our data (see §3.1).

3.1. SED templates

Our SED fitting procedures utilize the four empirical SED templates spanning $0.03 - 30 \mu\text{m}$ described in Assef et al. (2010a, A10 hereafter). A10 have shown that the non-negative combinations of three different galaxy templates and a single AGN template, with the addition of extinction to the AGN component only, can robustly describe the optical to mid-IR SEDs of a wide variety of AGNs selected using *Spitzer* IRAC color (Assef et al. 2010a) or *WISE* color (Assef et al. 2010b; Chung et al. 2014). However, these templates do not include the far-IR wavelengths that are crucial for this work.

To extend the A10 AGN template to the far-IR, we create *ad hoc* AGN templates by replacing the hot-dust component of the A10 AGN template with the average infrared quasar template from Netzer et al. (2007) and the three infrared AGN templates (for low-, mean-, and high-luminosity AGNs) from Mullaney et al. (2011), which cover a wide range of AGNs with different mid-IR to far-IR properties. This is based on the assumption that the SED of the hot accretion disk around the SMBH is the same for all the radiatively efficient AGNs, and that the differences are due to variable extinction and different spectral shapes in the mid- and far-IR wavelengths due to different distributions of dust. To account for the extinction at the AGN templates, we use the Draine (2003) extinction law with $R_V = 3.1$, which mainly attenuates the SED at $\lambda \leq 30 \mu\text{m}$ and also produces the silicate absorption features at mid-IR wavelengths that are common among AGN. The extinction strength is treated as a free parameter with a range of $0 < A_V < 48$.

For the host galaxy templates, we consider two different

¹³ Defined as the integrated $8 - 1000 \mu\text{m}$ luminosity of the host galaxy component only.

components: the contribution from the stellar population of the galaxy, which accounts for the optical to near-IR emission; and a starburst component, which represents the mid-to far-IR dust emission from re-processed stellar light. For the stellar population component, we follow the approach described in A10 by assuming that the stellar population in any galaxy is comprised of the non-negative combination of the three empirical galaxy templates with populations of starburst (Im), continuous star-forming (Sbc) and old stars (elliptical), respectively (Assef et al. 2008, 2010a). Unlike the elliptical template, the Sbc and Im templates both contain hot dust components in addition to the stellar population SEDs. Since the dust component does not extend to the far-IR wavelengths we require and will be taken into account in the starburst templates which we will choose later on, we replace the dust emission ($\lambda > 4.9 \mu\text{m}$) in the Sbc and Im templates with the SED identical to the elliptical galaxy to create empirical stellar population templates with no dust emission. At these wavelengths the stellar SEDs are dominated by low mass stars similar to the elliptical template. For our mid-IR selected quasar sample, the star light contribution is negligible at the wavelengths where hot dust emission dominates.

For the starburst component, we use the 105 starburst templates from Chary & Elbaz (2001) and the 64 starburst templates from Dale & Helou (2002). The Chary & Elbaz (2001) and Dale & Helou (2002) starburst templates cover a wide range of SEDs for various prototypical local star forming galaxies, with L_{IR} in the range between $10^8 - 10^{13.5} L_{\odot}$. For SF galaxies at $z > 1$, these templates have been shown to be reliable when used to estimate SF-related L_{IR} with monochromatic SPIRE observations (e.g. Elbaz et al. 2011). However, as pointed out by Kirkpatrick et al. (2012), the starburst galaxies at higher redshift have different dust temperatures and SED shapes. Although the effect of the different dust temperature on the estimation of $L_{\text{IR}}^{\text{SF}}$ is small when the wavelengths of the SPIRE bands probe the peak of the cold dust emission, it is still important to include high redshift starburst templates to accommodate the possibly different SED shapes of high redshift starbursts. Therefore, we also include the $z \sim 1$ and $z \sim 2$ average starburst SED templates from Kirkpatrick et al. (2012) in our SED fitting analysis. We thus adopt a total of 171 starburst templates in our SED fitting analysis.

Given these SED templates described above, we fit the observed photometry with an iterative χ^2 minimization algorithm (Levenberg-Marquardt) to minimize the function.

$$\chi^2 = \sum_{i=0}^{n_{\text{filters}}} \frac{F_{\text{obs},i} - aF_{\text{star},i} - b \text{ext}(E(B-V))F_{\text{AGN},i} - cF_{\text{starburst},i}}{\sigma_i^2} \quad (1)$$

Here $F_{\text{obs},i}$ is the observed flux in the i th band and σ_i is its uncertainty. $F_{\text{galaxy},i}$, $F_{\text{AGN},i}$ and $F_{\text{starburst},i}$ are the fluxes of the stellar (optical), AGN (optical to far-IR) and starburst (far-IR) templates for filter i . The function ext gives the extinction of the AGN flux in band i given the color excess $E(B-V)$. We optimize a, b, c and $E(B-V)$ to minimize the χ^2 .

3.2. Results

While uniform NUV to mid-IR photometric coverage is available for all of the sources in our sample, only $\sim 18\%$ of them have a SPIRE $250 \mu\text{m}$ detection with a flux larger

than the 20 mJy . Since our sample is selected to have AGN-dominated mid-IR SED, the far-IR photometry is essential to constrain the average SF properties. For the sources with direct far-IR detections, we fit their multiwavelength photometry with the SED templates described in the previous section. For the 731 sources without direct far-IR detections, we use a stacking analysis to constrain their average far-IR flux.

We stack the QSOs without direct far-IR detections in bins of $R - [4.5]$ (see §4.2) and bins of L_{AGN} (derived in H11 from interpolations between the IRAC photometry and the MIPS $24 \mu\text{m}$ photometry). The uncertainty of the stacked flux is determined by bootstrap resampling. We created 10,000 random samples by drawing objects from the original samples with replacement until the number of objects in each random sample is the same as the number in the original sample. The uncertainty of the stacked flux is the variation in the stacked fluxes of the random samples. The details of the far-IR stacking analysis can be found in §3.1.1 of Alberts et al. (2013). The results of the stacking analysis are given in Table 1.

To estimate the average SF luminosity of the far-IR non-detected QSOs, we assume that their $250 \mu\text{m}$ fluxes and $250 \mu\text{m}$ flux uncertainties are equal to the averages found from the stacking analysis for the sources with similar values of both $R - [4.5]$ and L_{AGN} . We find that for the majority of the SPIRE-non detected sample, the best-fitting SED reproduces the observed average far-IR flux well.

From SED fitting results with far-IR fluxes stacked in bins of $R - [4.5]$ and L_{AGN} , we find that $\sim 85\%$ of the quasars have a prominent AGN hot dust component (AGN component $> 50\%$) at mid-IR wavelengths covered by the IRAC bands. All of the quasars have a non-negligible ($> 20\%$) AGN component, confirming that the H11 sample consists of powerful quasars. However, the AGN dominates the quasar SED even at $24 \mu\text{m}$ for more than a half of our sample. So the SF properties of these powerful quasars is primarily constrained by their far-IR photometry. For individual sources with only the stacked SPIRE flux to anchor the starburst component, this approach of using stacked far-IR flux can lead to inaccurate $L_{\text{IR}}^{\text{SF}}$. However, the main purpose of this work is not to determine the $L_{\text{IR}}^{\text{SF}}$ for individual QSOs. Instead, we take this approach to constrain the AGN contamination in the average far-IR SF luminosity with the well-fitted mid-IR AGN SED, which can robustly determine the average $L_{\text{IR}}^{\text{SF}}$ for different QSO populations. We note that when we compare the stacked fluxes from either the $R - [4.5]$ bin or the L_{AGN} bin with the best-fitting AGN component, we find that the average AGN contribution at $250 \mu\text{m}$ is only 5% ; and none of the QSOs in our sample have an AGN component that contributes more than 40% at $250 \mu\text{m}$. Since the average intrinsic SEDs for AGNs are expected to fall more rapidly in more luminous systems (Mullaney et al. 2011), a starburst component is essential to reproduce to average flux at $250 \mu\text{m}$.

With the best-fitting SEDs, we calculate the total infrared luminosity for each QSO ($L_{\text{IR}}^{\text{tot}}$) by integrating the best-fitting SEDs from $8 - 1000 \mu\text{m}$. For each source in our sample, we also calculate the L_{IR} of the starburst component by integrating the host galaxy component of the best-fitting SED over the same wavelength range ($L_{\text{IR}}^{\text{SF}}$ hereafter)¹⁴. We find that for our sample, the average ratio between $L_{\text{IR}}^{\text{SF}}$ and $L_{\text{IR}}^{\text{tot}}$ is

¹⁴ For clarification, we use L_{IR} as a general terminology for any integrated $8 - 1000 \mu\text{m}$ luminosity. $L_{\text{IR}}^{\text{tot}}$ is the integrated L_{IR} of the best-fitting SED and $L_{\text{IR}}^{\text{SF}}$ is the L_{IR} of the host galaxy component only.

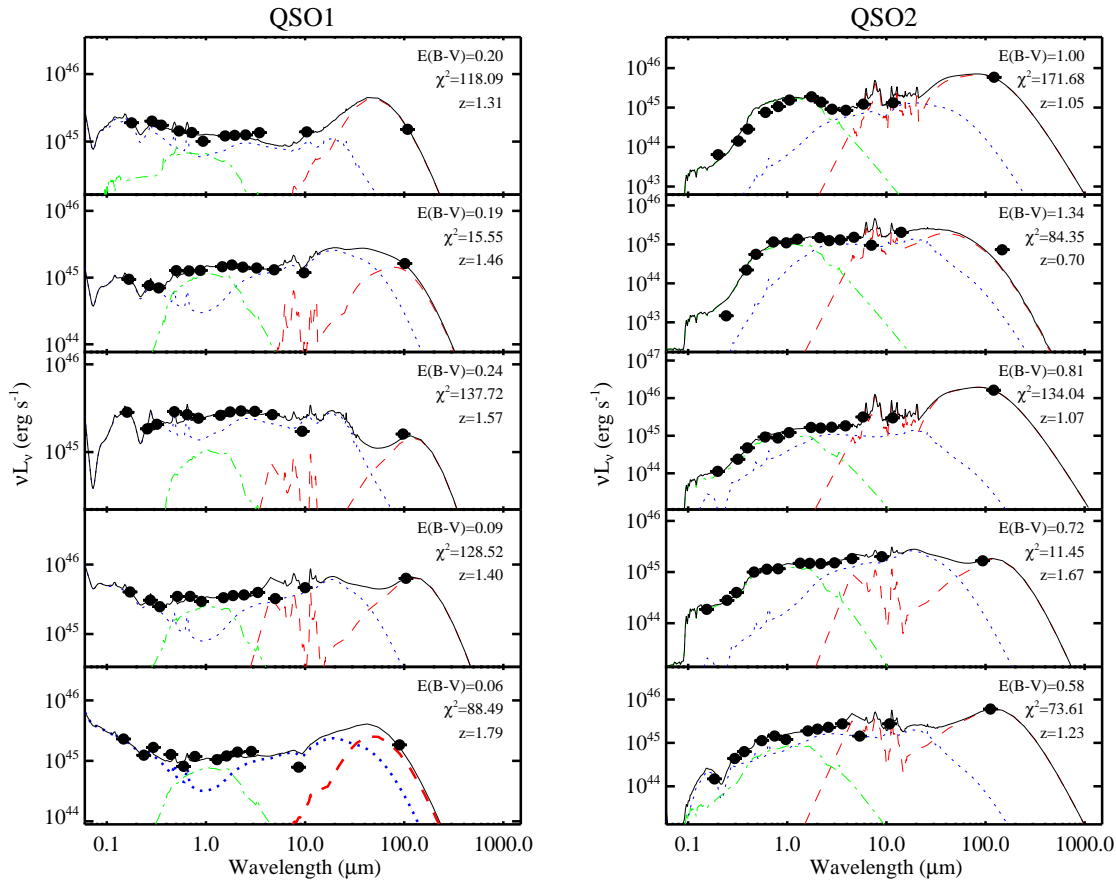


FIG. 3.— Examples of the best-fitting SEDs (solid line) in the rest-frame of each source. These sources are fitted using an AGN component with a Draine (2003) extinction law (dotted curve), an empirical stellar component (dash-dotted) and empirical starburst templates (dashed). We find that almost all sources have an SED dominated by the starburst component in the far-IR, see §3 for details.

$\sim 55\%$, indicative of a non-negligible AGN contribution to $L_{\text{IR}}^{\text{tot}}$ in these mid-IR luminous quasars. This is also consistent with the Kirkpatrick et al. (2012) results of the study combining *Spitzer* IRS spectra and multi-band *Herschel* photometry for $z \sim 1$ and $z \sim 2$ ULIRGs. However, the far-IR flux probed by the SPIRE 250 μm band is dominated ($> 70\%$) by the starburst component for $\sim 90\%$ of our sample. This result confirms that quasar SEDs are still dominated by a starburst component at rest-frame wavelengths longer than 100 μm (e.g. Netzer et al. 2007; Mullaney et al. 2011; Rosario et al. 2012; Del Moro et al. 2013). Therefore, the average $L_{\text{IR}}^{\text{SF}}$ of powerful mid-IR quasars can still be robustly measured with the inclusion of far-IR photometry.

We next derive the bolometric AGN luminosity (L_{AGN}) by directly integrating the de-absorbed AGN component. We compare the L_{AGN} from our SED fitting with the L_{AGN} derived in H11, and found that our L_{AGN} is higher than the H11 L_{AGN} by an average of ~ 0.1 dex. Since the derivation of L_{AGN} in H11 did not correct for the weak but non-negligible dust obscuration and SF galaxy contamination in the mid-IR, it is not surprising that our L_{AGN} is different. However, the difference is small due to the fact that most of the quasars in this sample are dominated by the AGN and the dust obscuration only weakly attenuates the SED at mid-IR wavelengths. We show the redshift distributions of $L_{\text{IR}}^{\text{tot}}$ and L_{AGN} in Fig. 4.

4. FAR-IR OBSERVATIONS AND QUASAR OBSCURATION

Several studies have pointed out that even for AGNs with quasar-like luminosities, their far-IR SEDs are often dom-

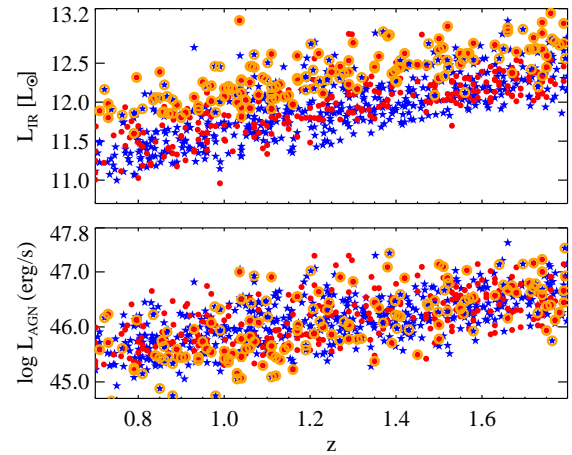


FIG. 4.— The redshift distributions of the (8–1000 μm) $L_{\text{IR}}^{\text{total}}$ and the AGN bolometric luminosity derived from SED fitting and far-IR stacking for non-detected sources described in §3.2. The symbols and lines represent the same subsets of objects shown in Fig. 1, where blue stars and red circles are QSO1s and QSO2s, respectively. Individually far-IR detected sources (FIR-QSO) are enclosed with orange circles.

inated by the cold dust emission heated by young stars (e.g. Netzer et al. 2007; Lacy et al. 2007a; Kirkpatrick et al. 2012; Mullaney et al. 2012). Although alternative cases have been reported in some recent studies (e.g. Hiner et al. 2009; Dai et al. 2012), the cold temperature of the far-IR emission still requires the AGN-heated dust to reside at a large distance

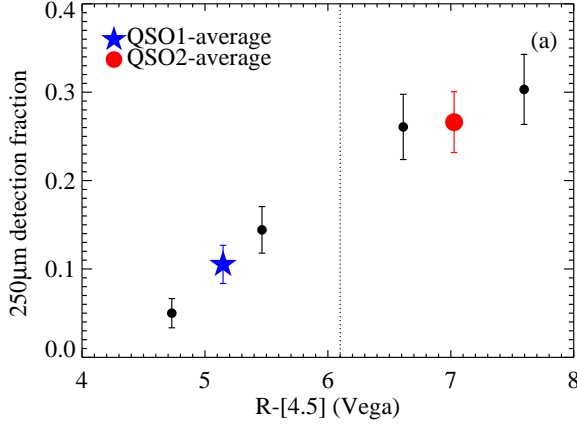


FIG. 5.— The 250 μm detection fraction (f_{250}) as a function of the $R-[4.5]$ color. The f_{250} for all QSO1s is shown as the blue star, and the f_{250} for all QSO2s (weighted to have a redshift and AGN bolometric luminosity distribution similar to that of QSO1s) is shown as the red circles. This figure shows that QSO2s are 2.4 times more likely to have a far-IR detection.

from the central SMBH (Sanders et al. 1988). In addition, powerful molecular outflows might also produce strong far-IR emission (e.g. Sun et al. 2014). However, the number of AGNs and starburst galaxies with confirmed warm molecular outflows from high-resolution far-IR or sub-mm observations is limited. Nonetheless, strong far-IR emission for quasars implies the existence of dust extending to a large distance well beyond the putative obscuring torus, and a comparison of far-IR properties between QSO1s and QSO2s could determine that whether the quasar obscuration is related to the large-scale dust.

4.1. SPIRE detection fraction

We begin with a very simple test by measuring the far-IR detection fraction above a flux limit of 20 mJy in the *Herchel* SPIRE 250 μm filter (f_{250} hereafter) for QSO1s and QSO2s separately. In our survey region, the shallowness of the SPIRE observation implies that any quasars in our sample with a far-IR detection are at least as bright as luminous infrared galaxies (LIRGs, which are defined as galaxies with $L_{\text{IR}}(8-1000 \mu\text{m}) > 10^{11} L_{\odot}$) at the same redshifts. At first glance, we find that among the 546 QSO1s, only 68 (12%) of them are detected in the SPIRE 250 μm filter, while 102 of the 345 (29%) QSO2s have far-IR detections.

We next use $R-[4.5]$ as a rough proxy of the obscuration strength on the nuclear emission and study whether f_{250} is related to the extinction at the R band. The primary goal of this analysis is to study whether the star formation properties of the quasar-hosting galaxies are related to the observed obscuration. Therefore, it is important to make sure the QSO1s and QSO2s are matched in key properties, i.e. redshift and AGN bolometric luminosity (L_{AGN} , estimated from the SED fitting analysis discussed in §3). We divide our sample into four bins of $R-[4.5]$ and calculate f_{250} for each bin by applying statistical weights to each quasar so that the samples are matched in redshift and L_{AGN} in each bin. We find that the weighted f_{250} increases rapidly with $R-[4.5]$ for QSO1s. For QSO2s, f_{250} is only weakly correlated with $R-[4.5]$, but the f_{250} of QSO2s is higher than that of QSO1s by a factor of 2.7 ± 0.2 . We show the f_{250} to $R-[4.5]$ relation in Fig. 5.

4.2. The average SPIRE 250 μm fluxes

Due to the flux limit of the SPIRE catalog, f_{250} only reflects the fraction of QSOs hosted by galaxies with very luminous far-IR emission. To extend this analysis, we estimate the average 250 μm flux in bins of $R-[4.5]$ to test if the far-IR flux of our quasar sample also evolves with $R-[4.5]$. To measure the average 250 μm flux (S_{250}) for all QSOs, we first estimate the average 250 μm flux for the sources without direct SPIRE observations using the stacking analysis discussed in §3.2. Next, the stacked fluxes is combine with the sources individually detected in far-IR to calculate the average S_{250} for all QSOs. We show the average 250 μm flux (S_{250}) in the same $R-[4.5]$ bins used for Figure 5, with results given in Table 1.

From the stacking analysis, we find that for QSOs without direct far-IR detections, there is no significant dependence of the average S_{250} on $R-[4.5]$. However, the mean S_{250} of the individually detected far-IR sources shows a $R-[4.5]$ dependence similar to that of f_{250} . Therefore, driven by the increasing fraction of far-IR luminous sources, the average S_{250} of the entire QSO sample is correlated with $R-[4.5]$.

This result shows that for powerful mid-IR quasars with more dust attenuation at optical wavelengths, the average far-IR emission is stronger. This implies that at least part of the obscuration seen in the obscured QSOs might be due to the far-IR emitting dust.

5. THE AVERAGE $L_{\text{IR}}^{\text{SF}}$ OF QSO1S AND QSO2S

In §3, we found that QSO2s have higher f_{250} and S_{250} than QSO1s. In this section, we examine whether the observed difference in the average far-IR fluxes of QSO1s and QSO2s can be associated with the difference in the star formation properties of their host galaxies, as predicted by the galaxy evolution models with a connection between quasar obscuration and star formation.

We first calculate the median star formation luminosity by averaging the $L_{\text{IR}}^{\text{SF}}$ derived from SED fitting (§4). We find that for QSO1s, the mean $L_{\text{IR}}^{\text{SF}}$ is $10^{45.29 \pm 0.03} \text{ erg s}^{-1}$ ($10^{11.71} L_{\odot}$); and for QSO2s, the mean $L_{\text{IR}}^{\text{SF}}$ is $10^{45.59 \pm 0.04} \text{ erg s}^{-1}$ ($10^{12.01} L_{\odot}$). We find that similar to f_{250} and the average S_{250} , the median $L_{\text{IR}}^{\text{SF}}$ for QSO2s is significantly higher than that of QSO1s by 0.30 dex. The higher $L_{\text{IR}}^{\text{SF}}$ in QSO2s confirms the results from §3 that QSO2s are associated with host galaxies with more star-forming cold dust which might be obscuring the nuclear emission.

5.1. $L_{\text{IR}}^{\text{SF}}$ vs. $R-[4.5]$

To further study the relation between AGN obscuration and $L_{\text{IR}}^{\text{SF}}$, we divide our QSO sample into bins of $R-[4.5]$ as a proxy for AGN obscuration. To be consistent with §3.1 and avoid the uncertainties by the lack of *spec-zs* of QSO2s, we opt to use $R-[4.5]$ instead of the $E(B-V)$ derived from SED fitting as the proxy for nuclear obscuration, since the uncertainties of the *photo-z* limit the accuracy of our ability to measure $E(B-V)$. We calculate the median AGN contribution at observed frame R and $[4.5]$ bands using the best-fitting SEDs in each bin. We find that towards redder $R-[4.5]$ colors, the AGN contributes 89%, 79%, 29%, 12% at the R band and 74%, 59%, 43%, 60% at the $[4.5]$ band. This suggests that the empirical $R-[4.5]$ color is indeed a good proxy of AGN obscuration at optical wavelengths, and that the QSO classification based on the $R-[4.5]$ color is reliable. We then calculate the average $L_{\text{IR}}^{\text{SF}}$ ($\langle L_{\text{IR}}^{\text{SF}} \rangle$) in bins of $R-[4.5]$. We again estimate the uncertainty in $\langle L_{\text{IR}}^{\text{SF}} \rangle$ using bootstrap resampling.

TABLE 1
RESULTS OF FAR-IR STACKING ANALYSIS

Average f_{250} in bins of $R-4.5$				
$R-4.5$ (Vega)	4.7	5.4	6.6	7.5
S_{250} (mJy) (ND)	6.58 ± 0.73	7.93 ± 0.59	7.39 ± 0.75	8.57 ± 1.00
S_{250} (mJy) (All)	8.04 ± 0.84	11.4 ± 0.77	16.4 ± 1.50	18.0 ± 0.21
$\langle z \rangle$ (all)	1.31	1.20	1.19	1.31
Average f_{250} in bins of L_{AGN}				
$\log \langle L_{\text{AGN}} \rangle$ [erg s $^{-1}$]	45.2	45.6	46.1	46.5
S_{250} (QSO1)(mJy)	3.76 ± 0.82	5.49 ± 0.70	5.21 ± 0.75	7.70 ± 0.95
S_{250} (QSO2)(mJy)	3.56 ± 0.94	8.84 ± 1.40	5.18 ± 0.66	8.44 ± 2.70
z (average)	0.98	1.17	1.36	1.49

NOTE. — Results from the far-IR stacking analysis described in §4.2. The top half of the table shows the results for sources binned in $R-4.5$. The first row shows the results for the far-IR non-detected (ND) sources only, and the second row shows the result for the entire QSO sample. The average redshift for all QSOs in each bin is also given. The bottom half of the table shows the results for the entire QSO1 and QSO2 samples binned in their AGN bolometric luminosity. The average redshift for each $R-4.5$ and L_{AGN} bin is also listed; we note that there is only a < 0.02 average redshift difference between the QSO1s and QSO2s.

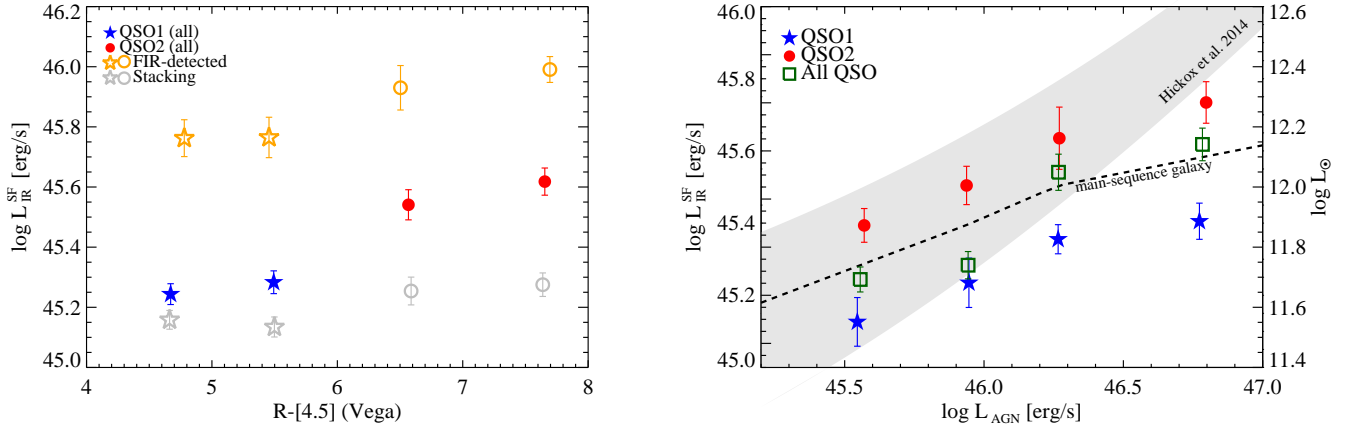


FIG. 6. — (a) *Left*: The relationship between $L_{\text{IR}}^{\text{SF}}$ and $R-4.5$ for the mid-IR selected QSOs. Far-IR detected QSOs are shown by the orange, open symbols and the stacking results for the far-IR non-detected QSOs are shown by the gray, open symbols. In both cases, there is only marginal increase in $L_{\text{IR}}^{\text{SF}}$ with $R-4.5$. However, driven by the much higher far-IR detection fraction in QSO2s, the average $L_{\text{IR}}^{\text{SF}}$ for QSO2s is higher than the average $L_{\text{IR}}^{\text{SF}}$ for QSO1. (b) *Right*: the average $L_{\text{IR}}^{\text{SF}}$ for QSOs in bins of L_{AGN} . The results for QSO1s are shown as the filled, blue stars; while the results for QSO2s are shown as the filled red circles. For the entire QSO population, we also show their average $L_{\text{IR}}^{\text{SF}}$ in four bins of L_{AGN} as the open, green squares. For comparison, we show the Hickox et al. (2014) model evaluated at $0.7 < z < 1.8$ as the shaded region. We note that the average redshift in each bin increases with L_{AGN} ; and the relationship between $\langle L_{\text{IR}}^{\text{SF}} \rangle$ and L_{AGN} is consistent with the redshift evolution for main-sequence SF galaxies with $M_* = 10^{11} M_{\odot}$. We show the redshift evolution of MS galaxies as the dashed line. The $L_{\text{IR}}^{\text{SF}}$ for all QSOs coincides with the evolution of MS galaxies, suggesting a connection between QSO host galaxies and MS star-forming galaxies (see §5.2).

We show the results in Fig. 6a. Even though the $L_{\text{IR}}^{\text{SF}}$ difference between QSO1s and QSO2s is large, $\langle L_{\text{IR}}^{\text{SF}} \rangle$ does not show the strong dependence on $R-4.5$ seen for f_{250} and the average S_{250} (Fig. 6a.) within QSO1s and QSO2s. Also, the $L_{\text{IR}}^{\text{SF}}$ difference between the far-IR detected QSO1s and QSO2s and the far-IR non-detected QSO1s and QSO2s are only 0.14 dex and 0.17 dex, which are not as significant as the 0.30 dex difference between all QSO1s and QSO2s. Thus the higher $\langle L_{\text{IR}}^{\text{SF}} \rangle$ of the QSO2 sample is mainly driven by its higher fraction of far-IR luminous SF galaxies.

5.2. $L_{\text{IR}}^{\text{SF}}$ vs. L_{AGN}

To explore the connections between AGN and host galaxy growth rates in different QSO populations, we separately divide the QSO1s and QSO2s into bins of L_{AGN} , and measure the $\langle L_{\text{IR}}^{\text{SF}} \rangle$ for each bin. The uncertainties are again estimated by bootstrapping as discussed in §5.1. We plot the $L_{\text{AGN}}-L_{\text{IR}}^{\text{SF}}$ relations for QSO1s and QSO2s in Fig. 6b. We find that both the QSO1 sample and the QSO2 sample have a positive $L_{\text{IR}}^{\text{SF}}-L_{\text{AGN}}$ correlation with similarly shallow

slopes, with $\log L_{\text{IR}}^{\text{SF}} \propto 0.25 \log L_{\text{AGN}}$ for QSO1s and $\log L_{\text{IR}}^{\text{SF}} \propto 0.27 \log L_{\text{AGN}}$ for QSO2s. However, the $\langle L_{\text{IR}}^{\text{SF}} \rangle$ for QSO2s is higher than that of QSO1s in each L_{AGN} bin by 0.28, 0.25, 0.32 and 0.28 dex.

For comparison, we also show the $L_{\text{AGN}}-L_{\text{IR}}^{\text{SF}}$ model from Hickox et al. (2014) which assumes a direct, linear correlation between the *average* L_{AGN} and $L_{\text{IR}}^{\text{SF}}$ while the observed L_{AGN} is modulated by rapid variability. We calculate the Hickox et al. (2014) relation spanning the $0.7 < z < 1.8$ redshift range in Fig. 6 as the shaded region. We find that for all QSO2s besides those in the most luminous L_{AGN} bin, our result is consistent with the H14 model, and the QSO1s have $L_{\text{IR}}^{\text{SF}}$ slightly lower than the model predictions throughout the entire L_{AGN} range. However, for both types of QSOs, the slope of the $L_{\text{IR}}^{\text{SF}}-L_{\text{AGN}}$ relation appears to be shallower than the prediction of the simple model if we take the different average redshift in each L_{AGN} bins into account.

As was shown by the results in Table 1, the average redshifts for more luminous QSOs are higher. Although our far-IR stacking approach can reliably measure the average far-IR fluxes and hence the average $L_{\text{IR}}^{\text{SF}}$, it is important to note that

the difference in the average redshift between the lowest and the highest L_{AGN} bins is 0.5, and it is possible that the observed correlation between $L_{\text{IR}}^{\text{SF}}$ and L_{AGN} is partially driven by the cosmic evolution of star formation and AGN accretion. Even though recent studies of the evolution of cosmic infrared luminosity density have shown that for the redshift range of the four L_{AGN} bins in Fig. 6b, the cosmic infrared luminosity is only weakly correlated with redshift ($\rho_{\text{IR}} \propto (1+z)^{-0.3 \pm 0.1}$ for $1.1 < z < 2.85$, Gruppioni et al. 2013), there is still a substantial evolution in the specific SFR (SFR per unit stellar mass) of “main sequence (MS)” SF galaxies (e.g. Elbaz et al. 2011).

A simple estimate of the effect of MS galaxy SFR redshift evolution can be made by calculating the average $L_{\text{IR}}^{\text{SF}}$ for MS galaxies with $M_{\star} = 10^{11} M_{\odot}$ at the redshift range of our QSO sample. From the theoretical framework of dark matter halo abundance matching methods (e.g. Behroozi et al. 2013), $10^{11} M_{\odot}$ is the typical galaxy stellar mass hosted by dark matter haloes of mass $M_{\text{halo}} = 10^{13.1} [h^{-1} M_{\odot}]$, which is the halo mass reported in recent clustering studies of mid-IR QSOs (e.g. Hickox et al. 2011; Donoso et al. 2014; DiPompeo et al. 2014). At the redshift of each QSO in our sample, the $L_{\text{IR}}^{\text{SF}}$ for a $10^{11} M_{\odot}$ MS galaxy can therefore be evaluated using the redshift-dependent SFR- M_{\star} relation from Whitaker et al. (2012) and a Kennicutt relation, $\text{SFR} = 1.09 \times L_{\text{IR}}^{\text{SF}} / L_{\odot}$ (Kennicutt 1998, modified for a Chabrier initial mass function). We find that the average $L_{\text{IR}}^{\text{SF}}$ for MS galaxies evaluated using this approach is consistent with the average $L_{\text{IR}}^{\text{SF}}$ in each L_{AGN} bin. This implies that for mid-IR quasars in this redshift range, the $L_{\text{IR}}^{\text{SF}}$ and instantaneous L_{AGN} might not be directly connected but still follow similar redshift evolution. This suggests that a common physical parameter (e.g. a common gas supply) might be driving the evolution of both SMBHs and galaxies. This is also consistent with the recent study of Rosario et al. (2013), which showed that the $L_{\text{IR}}^{\text{SF}} - L_{\text{AGN}}$ correlation for broad emission line QSOs is consistent with a scenario in which quasars are hosted by normal star-forming galaxies.

For mid-IR selected AGNs, contamination from star-forming galaxy interlopers is also an issue that might introduce biases to the measurements of AGN and star formation luminosities. While our SED fitting results show that 95% of the sources in our sample are indeed powerful QSOs with AGN-dominated mid-IR SED, it is still very important to verify that the observed $L_{\text{IR}}^{\text{SF}} - L_{\text{AGN}}$ relation in Fig. 6 is not caused by the incompleteness of our AGN selection criterion. In particular, a very powerful SF galaxy can harbor a heavily obscured AGN and still have starburst-like mid-IR SED. In such case, the IRAC color of the SF galaxy would fall out of the Stern et al. (2005) selection wedge (e.g. Kirkpatrick et al. 2012; Assef et al. 2010b; Chung et al. 2014), and the sample selected with the Stern et al. (2005) wedge would show a biased $L_{\text{IR}}^{\text{SF}} - L_{\text{AGN}}$ relation.

By happenstance, the mid-IR color of typical star-forming galaxy templates occupies the lower-left corner of the Stern et al. (2005) wedge at the redshift range of this sample (e.g. Donley et al. 2012, Fig. 17). Therefore, any AGN contribution in addition to the SF galaxy templates would easily promote a SF galaxy into the AGN identification wedge. This is particularly true for our sample of luminous quasars. We test this effect by first normalizing the $6 \mu\text{m}$ luminosity for AGN templates we used in the SED fitting described in §4 to $L_{\text{AGN}} = 10^{45} \text{ erg s}^{-1}$ to meet the minimum L_{AGN} crite-

riion of our QSO sample. We next combine these normalized AGN templates with two archetypical starburst galaxy templates, M82 and Arp 220 from Polletta et al. (2007). We find that to have a star forming galaxy falling out of the AGN identification wedge while having an $L_{\text{AGN}} \sim 10^{45} \text{ erg s}^{-1}$, its $L_{\text{IR}}^{\text{SF}}$ must exceed $10^{47} \text{ erg s}^{-1}$. This suggests that an SF galaxy must be a hyper-luminous infrared galaxies (HyLIRG, $L_{\text{IR}} > 10^{13} L_{\odot}$) to be able to hide an underlying quasar-like AGN component. According to the far-IR luminosity function of Gruppioni et al. (2013), there would only be less than 2 HyLIRGs in the redshift range of our sample given the size of the Boötes survey region. Because of the large number of sources in the lowest L_{AGN} bin of our sample, the inclusion of the 2 additional QSOs hidden in HyLIRGs would only affect the average $L_{\text{IR}}^{\text{SF}}$ by 0.15 dex, which is still within the 2σ range of the original L_{SF} .

We can also estimate biases in $L_{\text{IR}}^{\text{SF}}$ due to the sources not selected in the AGN identification wedge by examining the SEDs of the sources not classified as mid-IR QSOs. In the redshift range of our sample, there are 77 SPIRE-detected sources outside the Stern et al. (2005) wedge. When we fit the SEDs of these sources we find that most of these powerful SF galaxies have no significant AGN contribution in the mid-IR. For the sources without a mid-IR AGN component, we assume that AGN contributes $< 10\%$ to the mid-IR monochromatic luminosity at $6 \mu\text{m}$ as an upper limit. Only 4 of the 77 have L_{AGN} satisfying the $L_{\text{AGN}} > 10^{45} \text{ erg s}^{-1}$ criterion. If we add these four sources into the lowest L_{AGN} bin, the average $L_{\text{IR}}^{\text{SF}}$ would only increase by 0.05 dex. Therefore, we conclude that the $L_{\text{SF}} - L_{\text{AGN}}$ correlation observed in Fig. 6 is not biased by the exclusion of heavily obscured quasars hidden in powerful SF galaxies.

6. X-RAY PROPERTIES OF MID-IR QSOs

In §5, we have shown that for mid-IR selected QSOs, the AGN obscuration at optical wavelengths and the AGN mid-IR luminosity can both be connected to the star formation of their host galaxies. Here we use an alternative AGN accretion rate indicator, the X-ray emission, to study the interplay between the far-IR emitting dust and the X-ray emission.

We first count the number of detections in the far-IR and the X-ray observations. We note that the counts of X-ray detections can be affected by the varying sensitivity of the *Chandra* observations across the field (e.g. Mendez et al. 2013). However, the XBoötes observations are relatively uniform in depth ($\sim 4 - 8 \times 10^{-15} \text{ erg s}^{-1}$, Kenter et al. 2005) and this effect should be equivalent for both QSO types. The results of the detection fractions are summarized in Table 2. First, QSO1s have an X-ray detection fraction of 65%, which is much higher than the 12% far-IR detection fraction for QSO1s (see §3). For QSO2s, the X-ray detection fraction is only 34% while the far-IR detection fraction is 27%. We also find that the presence of far-IR emission is associated with lower X-ray detection fractions in both QSO1s and QSO2s. For QSO1s, 91% of the X-ray detected AGNs are not detected in the far-IR; while for QSO2s, 73% of the X-ray AGNs have no detectable far-IR emission. These number counts imply that large scale dust might also play an important role in the absorption of X-rays.

Since a large fraction ($\sim 76\%$) of the far-IR detected QSO2s have no direct X-ray detection, these far-IR bright QSO2s might not be included in an X-ray selected AGN sample. However, since both the far-IR and the X-ray observations

TABLE 2
NUMBER OF X-RAY DETECTED SOURCES

	N_X	N_{NX}	f_X	$\langle z \rangle$	$\log \langle L_{6\mu m} \rangle [\text{ergs}^{-1}]$	$\langle \log L_{\text{IR}}^{\text{SF}} \rangle [L_\odot]$	$\langle L_X \rangle [\text{erg s}^{-1}]$	$\langle A_V \rangle$
QSO1 (ALL)	356	190	0.65	1.24	46.20	11.74	44.17 ± 0.03	0.32
QSO1 (FIR)	30	35	0.46	1.26	46.38	12.21	43.93 ± 0.09	0.50
QSO1(No FIR)	326	155	0.67	1.24	46.17	11.62	44.19 ± 0.03	0.28
QSO2 (ALL)	119	235	0.34	1.26	46.25	12.06	43.78 ± 0.05	2.62
QSO2 (FIR)	23	74	0.24	1.24	46.27	12.34	43.66 ± 0.10	2.85
QSO2(No FIR)	87	161	0.35	1.26	46.24	11.80	43.82 ± 0.05	2.59

NOTE. — The number counts and properties of different subsamples of QSOs classified based on the X-ray and far-IR detections. The properties listed here are the number of sources with X-ray detections (N_X), the number of source without X-ray detections (N_{NX}), the X-ray detection fraction (f_X), the average redshift ($\langle z \rangle$), the average AGN bolometric luminosity ($\langle \log L_{\text{AGN}} \rangle$, see §4), the rest-frame 2–10 keV X-ray luminosity and A_V (see §4 and §5.3).

in our sample are relatively shallow, the detection fractions only reflect the incidence of bright starburst and bright X-ray AGNs. To compensate for the shallow flux limit of the XBoötes survey, we use an X-ray stacking analysis to estimate the average X-ray luminosity for the sources without direct X-ray detections. We defined the stacked X-ray counts as the average number of background-subtracted photons detected within the 90% point-spread function (PSF) energy encircled radius at 1.5 keV, r_{90} , where $r_{90} = 1'' + 10''(\theta/10')^2$. Here θ is the off-axis angle from the *Chandra* optical axis¹⁵. We adopt 3.0 and 5.0 counts $\text{s}^{-1} \text{deg}^{-2}$ for the diffuse X-ray background at 0.5–2 keV and 2–7 keV bands, which closely matches the average background in annuli after excluding detected X-ray sources. We refer to §5.1.1 of H07 and Chen et al. (2013) for details about X-ray stacking analysis.

We performed the analysis on the subsamples listed in Table 2. To calculate the average X-ray luminosity for each subsample of QSOs, we first calculate the rest-frame 2–10 keV L_X for each X-ray detected quasar from their observed 0.5–7 keV luminosity with a k -correction using the spectral index derived from the flux ratio between the soft (0.5–2 keV) and the hard (2–7 keV) bands. In detail, the X-ray spectrum was assumed to be a simple power-law and the hardness ratio was used to determine the power-law index (Γ) using PIMMS and the ACIS Cycle 4 on-axis response function. For the X-ray detected QSO1s, the average index is $\Gamma = 1.83$, which is typical for unabsorbed AGN X-ray spectra. For the X-ray detected QSO2s, the average index of $\Gamma = 1.24$ is consistent with AGNs with moderate absorbed spectra (Hickox et al. 2007). With the Γ derived from the observed hardness ratio, we k -corrected the observed-frame 0.5–7 keV luminosity to the rest-frame 2–10 keV, without de-absorbing the X-ray spectra. For the X-ray non-detected sources, we calculate their average rest-frame 2–10 keV L_X by k -correcting the stacked 0.5–7 keV luminosity derived from the stacked X-ray flux using the median redshift and the hardness ratio of stacked X-ray photons. The general X-ray properties of QSO1s and QSO2s have been discussed at length in §5 of Hickox et al. (2007). Combining the L_X of the individually X-ray detected sources with the average L_X for the non-detected sources from stacking, we obtain the average X-ray luminosities in Table 2. These X-ray luminosities are the observed values and are not corrected for absorption. We also list the median extinction A_V of the AGN template at optical wavelengths from the SED fitting results (see §4). For heavily obscured AGNs, the SED at optical wavelengths can be dominated by the host galaxy, and the average A_V may be a lower limit. However, we do find a much larger value of A_V for far-IR detected QSO1s than that for far-

IR non-detected QSO1s, which implies that the presence of star-forming dust attenuates both the optical and X-ray AGN emission.

We can also use the total numbers of stacked hard-band (2–7 keV) and soft-band (0.5–2 keV) photons to obtain the hardness ratio for different QSO subsamples. We find that for QSO1s, the HR remains a constant $HR \sim -0.42$ for both the far-IR detected and far-IR non-detected subsamples. While for QSO2s, the HR for both the far-IR detected and far-IR non-detected subsamples are also very similar ($HR \sim -0.12$). The large difference in the HR between QSO1s and QSO2s is consistent with the typical HR values for type I and type II X-ray AGNs, which has been demonstrated in H07. However, we here point out that the average hardness ratio is insensitive to the presence of far-IR emitting dust. The uniform HRs for far-IR detected and far-IR non-detected QSO2s might simply be due to the wide redshift distribution from which the stacked sources are drawn from, since the uncertainties of the measured HRs corresponds to more than 0.3 dex in N_H ($2-5 \times 10^{22} \text{cm}^{-2}$, e.g. Fig. 15 in H07) for the redshift range of our sample. However, the hardness ratios for the far-IR detected and far-IR non-detected QSO1s are both consistent with little or no neutral gas absorption, which cannot explain the large L_X difference between far-IR QSO1s and far-IR non-detected QSO1s. Therefore, the constant HR regardless of the presence of strong far-IR emissions might imply that the lower average L_X and the higher A_V in far-IR detected subsamples are due to gas of large column density that obscures X-ray photons in both hard-band and soft-band. We note that large columns of ionized gas residing within 10pc of the vicinity of the X-ray emitting corona might also absorb both the hard-band and soft-band photons without altering the observed HR. As demonstrated in various studies of X-ray spectral models (e.g. Ceballos & Barcons 1996), the observed hardness ratio is a much weaker function of the column density of the ionized warm absorber when compared to a neutral, cold absorber. This specific type of absorption has been observed in QSOs hosted by extremely luminous submillimeter galaxies (e.g. Page et al. 2011), similar to the luminous SF galaxies hosting QSO2s in this work. However, whether the same type of warm absorber exists in our far-IR detected QSOs cannot be confirmed without high-resolution X-ray spectroscopy.

We summarize the results of our stacking analysis in Fig. 7, where we show the ratio between $L_{6\mu m}$ and $\langle L_X \rangle$ for different subsamples of QSOs. Since L_X and L_{MIR} are both excellent tracers of SMBH accretion and L_{MIR} is relatively insensitive to obscuration, the L_X to L_{MIR} ratio has been used to track down the elusive population of Compton-thick AGNs and to study the intrinsic AGN accretion rate (e.g. Lutz et al. 2004; Alexander et al. 2008; Gandhi et al. 2009;

¹⁵ *Chandra* Proposers’s Observatory Guide (POG), available at <http://cxc.harvard.edu/proposer/POG>.

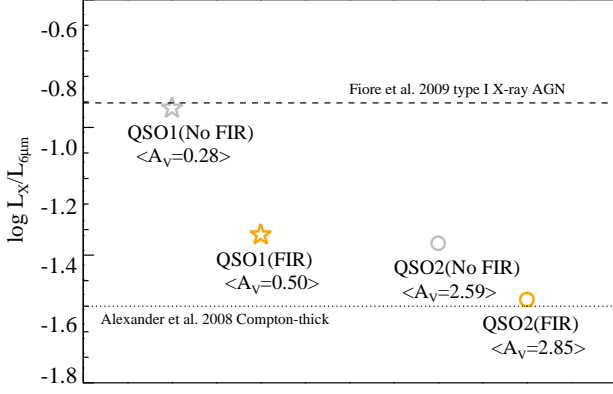


FIG. 7.— A summary of the $L_X/L_{6\mu m}$ for different QSO populations. For comparison, we show the $L_X/L_{6\mu m}$ relationship for type I X-ray AGNs using Eq. 2 from Fiore et al. (2009) evaluated at $L_{6\mu m} = 10^{44.9} \text{ erg s}^{-1}$ as the dashed line. We also show the $L_X/L_{6\mu m}$ relation for local AGNs with Compton-thick absorptions (Alexander et al. 2008) as the dotted line. We show that the presence of far-IR emitting dust attenuates the observed L_X in comparison to $L_{6\mu m}$ and increases the AGN extinction in the optical wavelengths. We note that far-IR luminous QSO2s might not be detected in wide-field X-ray surveys due to the heavy obscuration that can be associated with the dust-shrouded host galaxies.

Eckart et al. 2010; Goulding et al. 2011; Rovilos et al. 2013; Lansbury et al. 2014; Stern et al. 2014).

In Fig. 7, we show that for both QSO1s and QSO2s, the existence of a far-IR detection is connected with smaller $L_X/L_{6\mu m}$ ratios by at least 0.2 dex when compared to the far-IR non-detected subsamples. This indirectly supports a link between far-IR emitting dust and the absorption of X-ray photons. For comparison, we also show the luminosity-dependent $L_{6\mu m} - L_X$ relation by Fiore et al. (2009) evaluated at the average $L_{6\mu m}$ of our sample $L_{6\mu m} = 10^{44.9} \text{ erg s}^{-1}$. We find that the $L_X/L_{6\mu m}$ for QSO1s without direct far-IR detections is similar to the Fiore et al. (2009) relation. We note that for local active galaxies, an almost linear $L_{6\mu m} - L_X$ relation has been reported by several studies (e.g. Lutz et al. 2004; Maiolino et al. 2007; Gandhi et al. 2009), but the inferred $L_X/L_{6\mu m}$ value at $L_{6\mu m} = 10^{44.9} \text{ erg s}^{-1}$ would be -0.37 if we adopt Eq. 2 from Gandhi et al. (2009), which is much higher than the results for our far-IR non-detected QSO1s and the Fiore et al. (2009) relation. The X-ray hardness ratio of the QSO1 sample is consistent with little or no X-ray absorption, suggesting that the different $L_X/L_{6\mu m}$ ratios for QSOs and the X-ray selected AGNs (Fiore et al. 2009) observed are not simply due to the difference in gas absorption. The difference in the intrinsic mid-IR to X-ray spectral shape between local AGNs and quasars is beyond the scope of this work but will be addressed in a follow-up work by Chen et al. (2015, in preparation).

For AGNs with Compton-thick absorption, the observed L_X can be attenuated by a factor of more than 15 when compared to the intrinsic $L_{6\mu m} - L_X$ relation (e.g. Alexander et al. 2008; Goulding et al. 2010). We find that the $L_X/L_{6\mu m}$ of our far-IR detected QSO2s is consistent with the Alexander et al. (2008) relation derived from attenuating the X-ray luminosities for the $L_X/L_{6\mu m}$ relation of local AGNs (Lutz et al. 2004) with Compton-thick material. However, recent observations have also discovered several luminous AGNs with extremely weak X-ray emissions even in the ultra-hard energy bands probed by NuSTAR (Luo et al. 2013; Teng et al. 2014; Lansbury et al. 2014; Stern et al. 2014). Therefore, it is still

unclear whether the low $L_X/L_{6\mu m}$ ratio for the QSO2s is due to Compton-thick obscuration or intrinsic X-ray weakness. Nonetheless, the low $L_X/L_{6\mu m}$ for far-IR detected QSO2s is another line of evidence indicating that X-ray AGN selection methods can miss heavily obscured mid-IR QSOs hosted by galaxies with active SF activity. We caution that all AGN selection criteria suffer from various different selection biases, especially the incompleteness due to obscuration and the contamination from SF galaxy interlopers. We reiterate that SF galaxy contamination with our mid-IR color selection criteria is relatively mild for the shallow mid-IR flux limits of our sample. Our result demonstrates the advantage of mid-IR AGN selection criteria in detecting deeply obscured quasars hosted by powerful SF galaxies.

7. OBSCURED FRACTION AND $L_{\text{IR}}^{\text{SF}}$

In §5 and §6 we have shown that mid-IR selected QSO2s reside in galaxies with more active SF and that their AGNs are more obscured at both optical and X-ray wavelengths. While these results support the connection between AGN obscuration and star formation in the QSO host galaxies, we next directly test the connection between quasar obscuration and galaxy SF with the measurement of the “obscured fraction” as a function of $L_{\text{IR}}^{\text{SF}}$. We show this result in Fig. 8. For the far-IR detected QSOs, where $L_{\text{IR}}^{\text{SF}}$ can be more accurately estimated, we separate the sources into two bins of $L_{\text{IR}}^{\text{SF}}$ with equal number of sources in each bin. For the QSOs with $L_{\text{IR}}^{\text{SF}}$ estimated from stacked far-IR fluxes, the $L_{\text{IR}}^{\text{SF}}$ suffer from larger uncertainties. Therefore, we do not group these QSOs based on their $L_{\text{IR}}^{\text{SF}}$ but only evaluate obscured fractions for the entire populations. We find that the obscured fraction of the far-IR detected QSOs is much higher than that of the rest of QSOs, and the obscured fraction increases monotonically with respect to $L_{\text{IR}}^{\text{SF}}$ as $f_{\text{obs}} \propto 0.39 \times \log L_{\text{IR}}^{\text{SF}}$. This agrees with a scenario which connects the obscuration in powerful quasars to the host galaxy star formation, as the AGN unification model do not predict an increased obscured fraction for QSOs hosted by galaxies with higher $L_{\text{IR}}^{\text{SF}}$.

8. VERIFICATION OF THE DIFFERENCE BETWEEN QSO1S AND QSO2S

In this work, we have demonstrated that the star formation properties of QSO1s and QSO2s are different, which implies a link between star-forming dust and AGN obscuration in quasars. To verify the observed difference between QSO1s and QSO2 is not driven by the uncertainty of photometric redshifts of QSO2s and the presence of starburst contaminations, we perform several tests on the QSO1 sample and use the spectroscopically confirmed AGNs as a benchmark of how the various uncertainties might affect the observed properties of QSO2s.

8.1. Far-IR detection fraction

We reiterate that the sources with a dominating starburst component have been removed from the final sample studied in this analysis based on the SED fits discussed in §3. Therefore, the higher far-IR detection fraction for QSO2s is not due to the inclusion of starburst interlopers in the mid-IR AGN sample. Another possible issue that can drive the higher far-IR detection fraction for the QSO2s is the *photo-z* uncertainties. We here examine this issue by testing the null hypothesis that QSO1s and QSO2s have exactly the same far-IR detection fraction and redshift distribution.

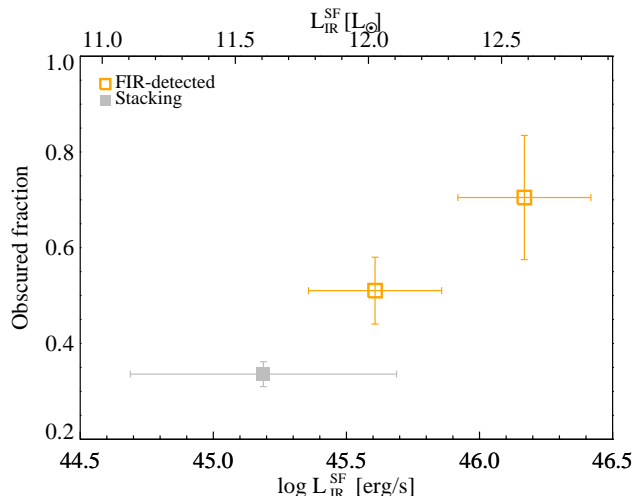


FIG. 8.— The obscured fraction (i.e. the QSO2 fraction) as a function of $L_{\text{IR}}^{\text{SF}}$. We separate far-IR detected QSOs into two bins of $L_{\text{IR}}^{\text{SF}}$ with equal number of sources in each bin, and plot their obscured fraction as the orange open squares. For the far-IR non-detected QSOs, we show the obscured fraction at the $L_{\text{IR}}^{\text{SF}}$ estimated from stacking analysis as the gray filled squares. The horizontal error bars show the inter-percentile range in $L_{\text{IR}}^{\text{SF}}$ containing 80% of the sample. This plot shows a monotonic increase of obscured fraction at higher $L_{\text{IR}}^{\text{SF}}$ which connects the AGN obscuration to the host galaxy star formation.

From the AGES catalog, we select all of the sources with broad emission lines (the BLAGNs). In the AGES catalog there are a total of 1619 BLAGNs of which 181 of them have a SPIRE 250 μm flux greater than 20 mJy. This far-IR detection fraction is similar to that for the QSO1 sample. To test if the uncertainties in photometric redshifts can boost the far-IR detection fraction, we randomly scatter the redshifts for all BLAGNs with the conservative uncertainty of $\sigma_z = 0.25(1+z)$ (discussed in §2.1). In each random realization, we select the sources with a randomly assigned redshift within $0.7 < z < 1.8$ and calculate their far-IR detection fraction. We repeat this process 100 times and found that on average, the random sample would have a far-IR detection fraction of only $\sim 9\%$. This means that the uncertainty in the photometric redshift would actually *decrease* the observed far-IR detection fraction if the far-IR luminosity function and the redshift distribution are the same for QSO1s and QSO2s. This is likely due to the negative k -correction at 250 μm for galaxies with typical cold dust SEDs (e.g. Blain 1996; Negrello et al. 2007). The starburst cold dust emission peaks at rest-frame $\sim 100 \mu\text{m}$ which correspond to the SPIRE 250 μm for an object at $z = 1.5$. Therefore, the starburst galaxies at lower redshifts are not brighter than our far-IR detected QSOs at observed-frame 250 μm due to the negative k -correction. High-redshift starbursts are also not likely to be included in our far-IR detected sample as the 250 μm filter probes the rapidly dropping Rayleigh-Jeans tail of the cold dust emission for objects beyond the redshift range of our sample.

Considering the significant difference of $\sim 17\%$ between the far-IR detection fractions of QSO1s and QSO2s, we confirm that the QSO2s are indeed more likely to be hosted by galaxies with strong far-IR emission than QSO1s.

8.2. Far-IR luminosity

Since the majority of QSO2s have only *photo-z*s and luminosity measurements are redshift dependent, it is of extreme

importance to confirm that the 0.3 dex average $L_{\text{IR}}^{\text{SF}}$ difference between QSO1s and QSO2s is not driven by solely by the uncertainty of *photo-z*s. Similar to the previous subsection, we estimate the effect of the *photo-z* uncertainty by testing the null-hypothesis that the QSO2s have the same $L_{\text{IR}}^{\text{SF}}$ distribution as the QSO1s. We again randomly assign redshifts to the AGES BLAGNs based on their *spec-z*s and the uncertainty upper limit $\sigma_z = 0.25(1+z)$. For the sources with a randomly assigned redshift within the $0.7 < z < 1.8$ range, we perform the SED analysis (described in §3) using the assigned redshift to calculate their average $L_{\text{IR}}^{\text{SF}}$. We repeat this process 100 times and found that the average $L_{\text{IR}}^{\text{SF}}$ difference between the random samples and the original QSO1 sample is 0.08 ± 0.02 dex, which is much smaller in comparison to the observed 0.3 dex difference between QSO1s and QSO2s. We also note that the $\sigma_z = 0.25(1+z)$ is a very conservative upper limit so the effects of photometric redshift uncertainty are almost certainly smaller. The L_{SF} difference between QSO1s and QSO2s is not driven by the *photo-z* uncertainty.

9. DISCUSSION AND SUMMARY

Recently, a number of studies of X-ray selected AGNs have found that star formation does not distinguish between AGNs with and without obscuration for AGNs classified based on either the presence of broad emission lines (Merloni et al. 2014) or the observed gas column density (N_{H} , e.g. Rovilos et al. 2012; Rosario et al. 2012). These conclusions are in direct contrast with our result in Fig. 6 showing a significant (> 0.25 dex) difference in $L_{\text{IR}}^{\text{SF}}$ between the QSO1s and the QSO2s.

To explain this apparent contradiction, we point out a fundamental difference between these studies and the present work. Merloni et al. (2014) classifies the X-ray selected AGN into “type 1” and “type 2” sources based SED fitting or the detection of broad emission lines. In our $R - [4.5]$ classification, all of the QSO1s are spectroscopically selected type 1 quasars, but it is not clear how many of our QSO2s would have spectra with narrow emission lines similar to that of the optical type 2 quasars; since the large amount of dust which blocks most of the AGN optical continuum might very well block the emission lines from the narrow line region essential to optical AGN classifications. Also, while deep X-ray and optical observations have proven to be efficient at detecting both obscured and unobscured AGNs, it is still challenging to include AGNs obscured by material with column density reaching $N_{\text{H}} \sim 5 \times 10^{24} \text{ cm}^{-2}$ (i.e. Compton thick) in optical or X-ray selected samples. Recent works on synthetic models of the cosmic X-ray backgrounds (e.g. Gilli et al. 2007; Treister et al. 2009; Ballantyne et al. 2011) suggest that a significant fraction of SMBH growth might occur in a heavily obscured, rapidly accreting AGN phase. As we have shown in Fig. 7, the far-IR detected QSO2s have a $L_X/L_{6\mu\text{m}}$ ratio consistent with AGNs that have heavily absorbed or intrinsically weak X-ray emission. Therefore, the different results might simply be due to mid-IR selected quasars representing different AGN populations than the optically and X-ray selected AGNs.

Indeed, mid-IR selection criteria have been shown to be capable of picking up sources with their nuclei obscured by Compton-thick material (e.g. Rovilos et al. 2013), and moderate-luminosity mid-IR AGNs have been found to preferentially populate the higher-end of AGN Eddington ratio distributions (e.g. Hickox et al. 2009), and to reside in more blue, star-forming host galaxies (e.g. Hickox et al. 2009;

Goulding et al. 2014). In conjunction with the higher $L_{\text{SF}}^{\text{IR}}$ and obscuration in our mid-IR quasars, we argue that part of the enhancement in $L_{\text{IR}}^{\text{SF}}$ of our sample when compared to X-ray or optical quasars is due to having different AGN populations based on different selection criteria and the heavy obscuration which possibly takes place on the scale of the host galaxy.

In summary, we have studied mid-IR luminous quasars at $0.7 < z < 1.8$ and demonstrated a connection between obscuration in mid-IR selected QSOs and star formation of their host galaxies. This connection is supported by the higher AGN obscured fraction in QSO host galaxies with larger $L_{\text{IR}}^{\text{SF}}$ and the large differences in the average far-IR luminosities between QSO1s and QSO2s. We have also shown that both the AGN obscuration at optical wavelengths and the AGN absorption at X-ray wavelengths can be connected to the presence of far-IR emitting dust. These results suggest that the large scale gas and dust are also obscuring the central AGNs in addition to orientation-based small-scale obscuration, which is consistent with the scenario in which the rapidly growing SMBHs

are connected to dust-enshrouded starburst galaxies.

We thank the anonymous referee for a careful reading of the manuscript and helpful suggestions that strengthened this paper greatly. We thank our colleagues on the AGES, ISS, SDWFS, NDWFS and the XBoötes teams, and the HerMES team for making the data publicly available. The first *Spitzer* MIPS survey of the Boötes region was obtained using GTO time provided by the *Spitzer* Infrared Spectrograph Team (PI: James Houck) and by M. Rieke. We thank the collaborators in that work for access to the 24 μm catalog generated from those data by Emeric LeFloc’h. This work was supported under contract NAS8-03060. R.J.A. was supported by Gemini-CONICYT grant number 32120009. C.-T.J.C., K.N.H. and R.C.H. were partially supported by the National Science Foundation through grant No. 1211096. K.N.H. and R.C.H. were partially supported by NASA through ADAP award NNX12AE38G. R.C.H. acknowledges support from an Alfred P. Sloan Research Fellowship and Dartmouth Class of 1962 Faculty Fellowship. C.-T.J.C. was supported by a Dartmouth Fellowship and the William H. Neukom 1964 Institute for Computational Science.

REFERENCES

- Alberts, S., Pope, A., Brodwin, M., et al. 2013, *MNRAS*, -1, 2563
 Alexander, D. M., Chary, R., Pope, A., et al. 2008, *ApJ*, 687, 835
 Alexander, D. M., Bauer, F. E., Brandt, W. N., et al. 2011, *ApJ*, 738, 44
 Antonucci, R. 1993, *ARA&A*, 31, 473
 Ashby, M. L. N., Stern, D., Brodwin, M., et al. 2009, *ApJ*, 701, 428
 Assef, R. J., Kochanek, C. S., Brodwin, M., et al. 2008, *ApJ*, 676, 286
 —. 2010a, *ApJ*, 713, 970
 Assef, R. J., Kochanek, C. S., Ashby, M. L. N., et al. 2010b, *ApJ*, 772, 26
 —. 2011, *ApJ*, 728, 56
 Baldwin, J. A., Phillips, M. M., & Terlevich, R. 1981, *PASP*, 93, 5
 Ballantyne, D. R., Draper, A. R., Madsen, K. K., Rigby, J. R., & Treister, E. 2011, *ApJ*, 736, 56
 Behroozi, P. S., Wechsler, R. H., & Conroy, C. 2013, *ApJ*, 770, 57
 Blain, A. W. 1996, *MNRAS*, 283, 1340
 Brodwin, M., Brown, M. J. I., Ashby, M. L. N., et al. 2006, *ApJ*, 651, 791
 Brown, M. J. I., Dey, A., Jannuzi, B. T., et al. 2007, *ApJ*, 654, 858
 Brusa, M., Comastri, A., Gilli, R., et al. 2008, *ApJ*, 693, 36
 Burlon, D., Ajello, M., Greiner, J., et al. 2011, *ApJ*, 728, 58
 Canalizo, G., & Stockton, A. 2001, *ApJ*, 555, 719
 Ceballos, M. T., & Barcons, X. 1996, *MNRAS*, 282, 493
 Chapin, E. L., Chapman, S. C., Coppin, K. E., et al. 2011, *MNRAS*, 411, 505
 Chary, R., & Elbaz, D. 2001, *ApJ*, 556, 562
 Chen, C.-T. J., Hickox, R. C., Alberts, S., et al. 2013, *ApJ*, 773, 3
 Chung, S. M., Kochanek, C. S., Assef, R., et al. 2014, *ApJ*, 790, 54
 Dai, Y. S., Bergeron, J., Elvis, M., et al. 2012, *ApJ*, 753, 33
 Dale, D. A., & Helou, G. 2002, *ApJ*, 576, 159
 Del Moro, A., Alexander, D. M., Mullaney, J. R., et al. 2013, *A&A*, 549, A59
 Di Matteo, T., Springel, V., & Hernquist, L. 2005, *Nature*, 433, 604
 DiPompeo, M. A., Myers, A. D., Brotherton, M. S., Runnoe, J. C., & Green, R. F. 2014, *ApJ*, 787, 73
 Donley, J. L., Rieke, G. H., Rigby, J. R., & Pérez-González, P. G. 2005, *ApJ*, 634, 169
 Donley, J. L., Koekemoer, A. M., Brusa, M., et al. 2012, *ApJ*, 748, 142
 Donoso, E., Yan, L., Stern, D., & Assef, R. J. 2014, *ApJ*, 789, 44
 Draine, B. T. 2003, *ARA&A*, 41, 46
 Drouart, G., De Breuck, C., Vernet, J., et al. 2014, *A&A*, 566, A53
 Eckart, M. E., McGreer, I. D., Stern, D., Harrison, F. A., & Helfand, D. J. 2010, *ApJ*, 708, 584
 Eisenhardt, P. R., Stern, D., Brodwin, M., et al. 2004, *ApJS*, 154, 48
 Elbaz, D., Dickinson, M., Hwang, H. S. S., et al. 2011, *A&A*, 533, A119
 Fiore, F., Puccetti, S., Brusa, M., et al. 2009, *ApJ*, 693, 447
 Gandhi, P., Horst, H., Smette, A., et al. 2009, *A&A*, 502, 457
 Georgantopoulos, I., Comastri, A., Vignali, C., et al. 2013, *A&A*, 555, A43
 Gilli, R., Comastri, A., & Hasinger, G. 2007, *A&A*, 463, 79
 Gonzalez, A. H., Brodwin, M., Brown, M. J. I., et al. 2010, *American Astronomical Society*
 Goulding, A. D., & Alexander, D. M. 2009, *MNRAS*, 398, 1165
 Goulding, A. D., Alexander, D. M., Mullaney, J. R., et al. 2010, *MNRAS*, 411, 1231
 —. 2011, *MNRAS*, 411, 1231
 Goulding, A. D., Forman, W. R., Hickox, R. C., et al. 2014, *ApJ*, 783, 40
 Griffin, M. J., Abergel, A., Abreu, A., et al. 2010, *A&A*, 518, L3
 Griffith, R. L., & Stern, D. 2010, *AJ*, 140, 533
 Gruppioni, C., Pozzi, F., Rodighiero, G., et al. 2013, *MNRAS*, -1, 32
 Guainazzi, M., Matt, G., & Perola, G. C. 2005, *A&A*, 444, 119
 Hainline, K. N., Hickox, R. C., Carroll, C. M., et al. 2014, *ApJ*, 795, 124
 Harrison, C. M., Alexander, D. M., Mullaney, J. R., et al. 2012, *ApJ*, 760, L15
 Harrison, F. A., Craig, W. W., Christensen, F. E., et al. 2013, *ApJ*, 770, 103
 Hickox, R. C., Mullaney, J. R., Alexander, D. M., et al. 2014, *ApJ*, 782, 9
 Hickox, R. C., Jones, C., Forman, W. R., et al. 2007, *ApJ*, 671, 1365
 —. 2009, *ApJ*, 696, 891
 Hickox, R. C., Myers, A. D., Brodwin, M., et al. 2011, *ApJ*, 731, 117
 Hiner, K. D., Canalizo, G., Lacy, M., et al. 2009, *ApJ*, 706, 508
 Hopkins, P. F., Hernquist, L., Cox, T. J., et al. 2006, *ApJS*, 163, 1
 Jannuzi, B. T., & Dey, A. 1999, in *ASP Conf. Ser. 191: Photometric Redshifts and the Detection of High Redshift Galaxies*, ed. R. Weymann, L. Storrie-Lombardi, M. Sawicki, & R. Brunner (San Francisco: ASP), 111
 Kennicutt, R. C. 1998, *ARA&A*, 36, 189
 Kenter, A., Murray, S. S., Forman, W. R., et al. 2005, *ApJS*, 161, 9
 Kirkpatrick, A., Pope, A., Alexander, D. M., et al. 2012, *ApJ*, 759, 139
 Kirkpatrick, A., Pope, A., Charmandaris, V., et al. 2013, *ApJ*, 763, 123
 Kochanek, C. S., Eisenstein, D. J., Cool, R. J., et al. 2012, *ApJS*, 200, 8
 Lacy, M., Petric, A. O., Sajina, A., et al. 2007a, *AJ*, 133, 186
 Lacy, M., Ridgway, S. E., Gates, E. L., et al. 2013, *ApJS*, 24
 Lacy, M., Sajina, A., Petric, A. O., et al. 2007b, *ApJ*, 669, L61
 Lacy, M., Storrie-Lombardi, L. J., Sajina, A., et al. 2004, *ApJS*, 154, 166
 Lansbury, G. B., Alexander, D. M., Moro, A. D., et al. 2014, *ApJ*, 785, 17
 Luo, B., Brandt, W. N., Alexander, D. M., et al. 2013, *ApJ*, 772, 153
 Lutz, D., Maiolino, R., Spoon, H. W. W., & Moorwood, A. F. M. 2004, *A&A*, 418, 465
 Mainieri, V., Bongiorno, A., Merloni, A., et al. 2011, *A&A*, 535, A80
 Maiolino, R., Shemmer, O., Imanishi, M., et al. 2007, *A&A*, 468, 979
 Mateos, S., Alonso-Herrero, A., Carrera, F. J., et al. 2013, *MNRAS*, 434, 941
 Mendez, A. J., Coil, A. L., Aird, J., et al. 2013, *ApJ*, 770, 40
 Merloni, A., Bongiorno, A., Brusa, M., et al. 2014, *MNRAS*, 437, 3550
 Mullaney, J. R., Pannella, M., Daddi, E., et al. 2012, *MNRAS*, 419, 95
 Mullaney, J. R., Alexander, D. M., Goulding, A. D. D., & Hickox, R. C. C. 2011, *MNRAS*, 414, 1082
 Murray, S. S., Kenter, A., Forman, W. R., et al. 2005, *ApJS*, 161, 1

- Negrello, M., Perrotta, F., Gonzalez, J. G.-N., et al. 2007, *MNRAS*, 377, 1557
- Netzer, H. 2009, *MNRAS*, 399, 1907
- Netzer, H., Lutz, D., Schweitzer, M., et al. 2007, *ApJ*, 666, 806
- Oliver, S. J., Bock, J., Altieri, B., et al. 2012, *MNRAS*, 424, 1614
- Page, M. J., Carrera, F. J., Stevens, J. A., Ebrero, J., & Blustin, A. J. 2011, *MNRAS*, 416, 2792
- Page, M. J., Stevens, J. A., Ivison, R. J., & Carrera, F. J. 2004, *ApJ*, 611, L85
- Page, M. J., Symeonidis, M., Vieira, J. D., et al. 2012, *Nature*, 485, 213
- Park, S. Q., Barmby, P., Willner, S. P., et al. 2010, *ApJ*, 717, 1181
- Polletta, M., Tajer, M., Maraschi, L., et al. 2007, *ApJ*, 663, 81
- Polletta, M. d. C., Wilkes, B. J., Siana, B., et al. 2006, *ApJ*, 642, 673
- Rosario, D., Santini, P., Lutz, D., et al. 2012, *A&A*, 545, A45
- Rosario, D. J., Trakhtenbrot, B., Lutz, D., et al. 2013, *A&A*, 560, A72
- Rovilos, E., Comastri, A., Gilli, R., et al. 2012, *A&A*, 546, A58
- Rovilos, E., Georgantopoulos, I., Akylas, A., et al. 2013, *MNRAS*, -1, 2867
- Sanders, D. B., Soifer, B. T., Elias, J. H., et al. 1988, *ApJ*, 325, 74
- Sazonov, S., Willner, S. P., Goulding, A. D., et al. 2012, *ApJ*, 757, 181
- Schawinski, K., Simmons, B. D., Urry, C. M., Treister, E., & Glikman, E. 2012, *MNRAS*, 425, L61
- Serjeant, S., & Hatziminaoglou, E. 2009, *MNRAS*, 397, 265
- Shan, H. G., & Chen, P. S. 2012, *MNRAS*, 421, no
- Silverman, J. D., Lamareille, F., Maier, C., et al. 2009, *ApJ*, 696, 396
- Somerville, R. S., Hopkins, P. F., Cox, T. J., Robertson, B. E., & Hernquist, L. 2008, *MNRAS*, 391, 481
- Stern, D., Eisenhardt, P., Gorjian, V., et al. 2005, *ApJ*, 631, 163
- Stern, D., Lansbury, G. B., Assef, R. J., et al. 2014, *ApJ*, 794, 102
- Sturm, E., Hasinger, G., Lehmann, I., et al. 2006, *ApJ*, 642, 81
- Sun, A.-L., Greene, J. E., Zakamska, N. L., & Nesvadba, N. P. H. 2014, *ApJ*, 790, 160
- Teng, S. H., Brandt, W. N., Harrison, F. A., et al. 2014, *ApJ*, 785, 19
- Treister, E., Urry, C. M., & Virani, S. 2009, *ApJ*, 696, 110
- Urry, C. M., & Padovani, P. 1995, *PASP*, 107, 803
- Usman, S. M., Murray, S. S., Hickox, R. C., & Brodwin, M. 2014, *ApJ*, 788, L3
- Whitaker, K. E., van Dokkum, P. G., Brammer, G., & Franx, M. 2012, *ApJ*, 754, L29
- Wilkes, B. J., Kuraszkiewicz, J., Haas, M., et al. 2013, *ApJ*, 773, 15
- Wright, E. L., Eisenhardt, P. R. M., Mainzer, A. K., et al. 2010, *AJ*, 140, 1868
- Zakamska, N. L., Gómez, L., Strauss, M. A., & Krolik, J. H. 2008, *AJ*, 136, 1607
- Zakamska, N. L., Strauss, M. A., Krolik, J. H., et al. 2006, *AJ*, 132, 1496